Article

Structural diversity of the SARS-CoV-2 Omicron spike

Graphical abstract
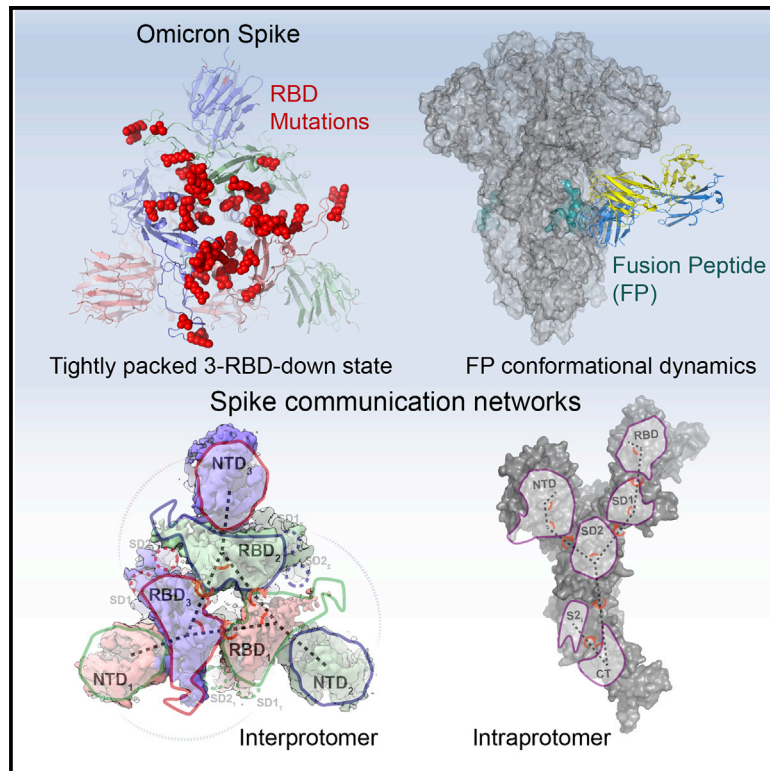
Authors

Sophie M.-C. Gobeil, Rory Henderson, Victoria Stalls, ..., Bette Korber, Barton F. Haynes, Priyamvada Acharya

Correspondence

barton.haynes@duke.edu (B.F.H.), priyamvada.acharya@duke.edu (P.A.)

In brief

Gobeil, Henderson, Stalls et al. identify diverse Omicron S ectodomain conformations demonstrating altered architecture that exhibits tight packing of the 3-RBD-down state, NTD-to-RBD (N2R) linker rearrangements, and changes in fusion peptide conformational dynamics. These distinct conformational features of its S protein may underlie Omicron's higher transmissibility and immune evasion.

Highlights

- Omicron S architecture differs from Delta and other variants

- Tight packing of Omicron S RBDs results in unique up- and down-state arrangements

- 3-RBD-down Omicron S stabilizes the rearrangement of the NTD-to-RBD (N2R) linker

- S2 subunit conformational changes lead to altered fusion peptide dynamics

CellPress

Article

Structural diversity of the SARS-CoV-2 Omicron spike

Sophie M.-C. Gobeil,[1,7] Rory Henderson,[1,2,7] Victoria Stalls,[1,7] Katarzyna Janowska,[1] Xiao Huang,[1] Aaron May,[1,3] Micah Speakman,[1] Esther Beaudoin,[1] Kartik Manne,[1] Dapeng Li,[1] Rob Parks,[1] Maggie Barr,[1] Margaret Deyton,[1] Mitchell Martin,[1] Katayoun Mansouri,[1] Robert J. Edwards,[1,2] Amanda Eaton,[1] David C. Montefiori,[1,4] Gregory D. Sempowski,[1,2] Kevin O. Saunders,[1,4] Kevin Wiehe,[1,2] Wilton Williams,[1,4] Bette Korber,[5] Barton F. Haynes,[1,2,6,*] and Priyamvada Acharya[1,3,4,8,*]

[1]Duke Human Vaccine Institute, Durham, NC 27710, USA
[2]Department of Medicine, Duke University, Durham, NC 27710, USA
[3]Department of Biochemistry, Duke University, Durham, NC 27710, USA
[4]Department of Surgery, Duke University, Durham, NC 27710, USA
[5]Theoretical Biology and Biophysics, Los Alamos National Laboratory, Los Alamos, NM 87545, USA
[6]Department of Immunology, Duke University, Durham, NC 27710, USA
[7]These authors contributed equally
[8]Lead contact
*Correspondence: barton.haynes@duke.edu (B.F.H.), priyamvada.acharya@duke.edu (P.A.)
https://doi.org/10.1016/j.molcel.2022.03.028

SUMMARY

Aided by extensive spike protein mutation, the SARS-CoV-2 Omicron variant overtook the previously dominant Delta variant. Spike conformation plays an essential role in SARS-CoV-2 evolution via changes in receptor-binding domain (RBD) and neutralizing antibody epitope presentation, affecting virus transmissibility and immune evasion. Here, we determine cryo-EM structures of the Omicron and Delta spikes to understand the conformational impacts of mutations in each. The Omicron spike structure revealed an unusually tightly packed RBD organization with long range impacts that were not observed in the Delta spike. Binding and crystallography revealed increased flexibility at the functionally critical fusion peptide site in the Omicron spike. These results reveal a highly evolved Omicron spike architecture with possible impacts on its high levels of immune evasion and transmissibility.

INTRODUCTION

The SARS-CoV-2 Omicron (B.1.1.529) variant was identified on November 24th, 2021 in South Africa, declared a variant of concern (VOC) by the World Health Organization on November 26th, and has rapidly replaced Delta (B.1.617.2) as the dominant form of SARS-CoV-2 circulating globally. The Omicron spike (S) protein harbors 30 mutations and is the most immune-evasive VOC identified thus far, surpassing Beta (B.1.351) in its ability to resist neutralization by antibodies (Abs) (Figure S1) (Schmidt et al., 2022; Hoffmann et al., 2022; Cameroni et al., 2022; Planas et al., 2022). Structural studies have been instrumental in revealing changes in VOC S protein conformations and in understanding the atomic level mechanisms that drive higher transmissibility and immune evasion (Gobeil et al., 2021b; Cai et al., 2021; McCallum et al., 2021a, 2021c; Zhang et al., 2021).

The pre-fusion SARS-CoV-2 S protein is composed of the S1 and S2 subunits that undergo structural changes to facilitate receptor binding and fusion with the host-cell membrane (Wrapp et al., 2020; Walls et al., 2020). While the S2 subunit is conformationally stable prior to receptor engagement, the S1 subunit, with

its mobile N-terminal domain (NTD) and receptor-binding domain (RBD), is inherently dynamic. The RBD transitions between a "closed" ("down") state, where the binding site for the ACE2 receptor is occluded, and an "open" ("up") state that exposes the ACE2 binding site (Walls et al., 2020; Wrapp et al., 2020). Following receptor binding and proteolytic processing of the S protein, the S2 subunit undergoes large conformational changes that result in release of the fusion peptide (FP) to mediate fusion of the virus and host-cell membranes. RBD dynamics are impacted by inter-protomer RBD-to-RBD and RBD-to-NTD contacts, as well as by other S protein structural units, including the SD1 and SD2 subdomains and the "N2R (NTD-to-RBD) linker" that connects the NTD and RBD within a protomer. We previously described how the S1 domain interactions are modulated by VOCs to alter the S protein RBD presentation and how these can be exploited for immunogen design (Gobeil et al., 2021a, 2021b; Henderson et al., 2020).

Here, we determine structures of native, unstabilized Omicron and Delta S protein ectodomains to understand how the acquired mutations alter their conformational states and influence receptor-binding site and Ab epitope presentation. The
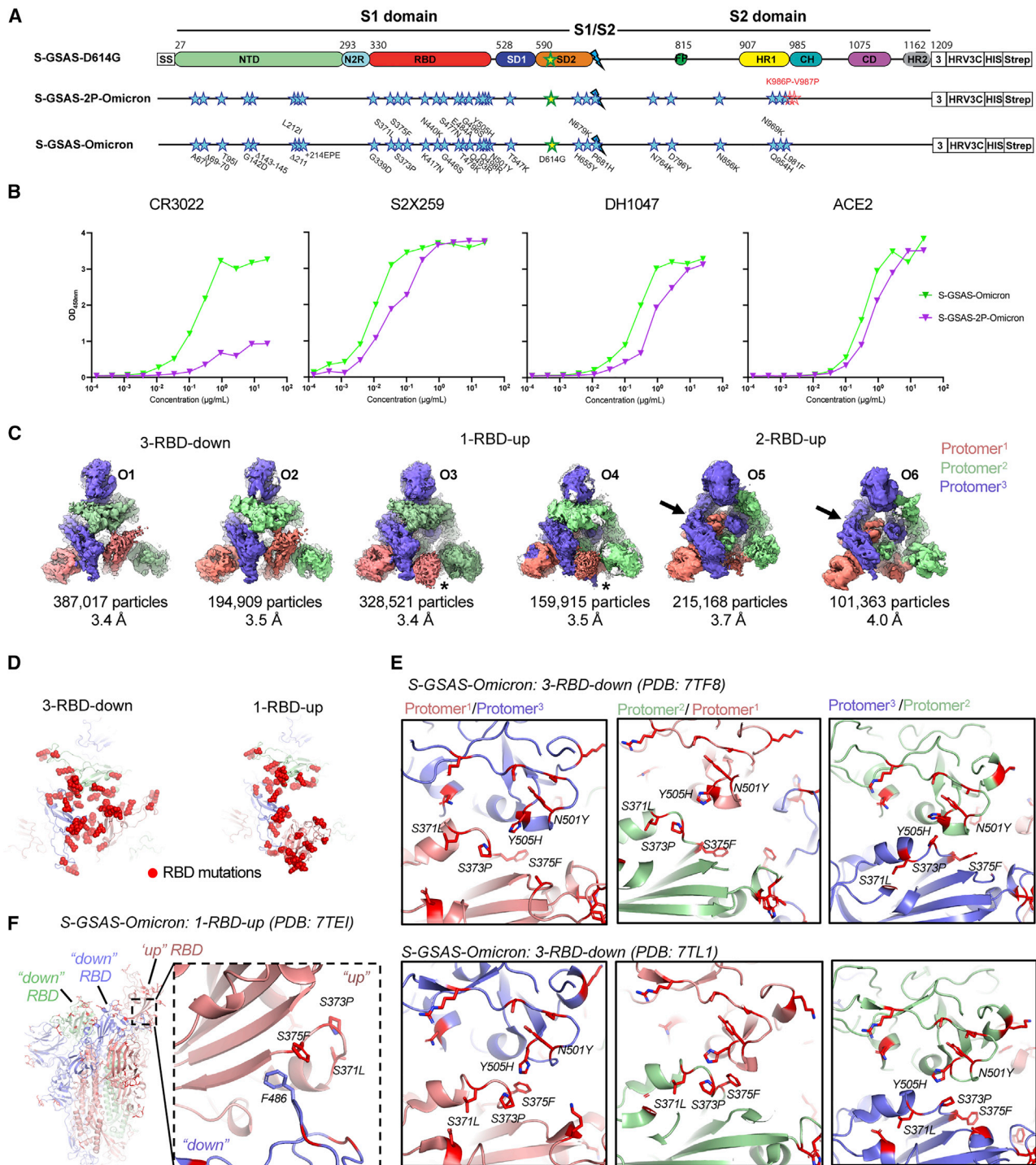
Figure 1. Conformational diversity of the SARS-CoV-2 Omicron (B.1.1.529) S protein

(A) Domain architecture of the SARS-CoV-2 S protomer. The S1 subunit contains a signal sequence (SS), the N-terminal domain (NTD) (pale green), NTD-to-RBD (N2R) linker (cyan), receptor-binding domain (RBD) (red), and subdomains 1 (SD1) and 2 (SD2) (dark blue and orange). The S2 subunit contains the fusion peptide (FP) (dark green), heptad repeat 1 (HR1) (yellow), central helix (CH) (teal), connector domain (CD) (purple), and heptad repeat 2 (HR2) (gray) subdomains. The transmembrane domain (TM) and cytoplasmic tail (CT) are replaced by a foldon trimerization sequence, followed by a HRV3C cleavage site (HRV3C), a histidine-tag (His), and a Strep-tag (Strep). The D614G mutation in SD2 is indicated by a yellow star with green contour. The location of the S1/S2 furin cleavage site (RRAR mutated to GSAS) is indicated by a blue lightning sign. The K986P-V987P mutations between the HR1 and CH domains in S-GSAS-2P-Omicron are indicated by red stars.

(legend continued on next page)

S ectodomains were prepared in our previously described S-GSAS-D614G platform without S2 subunit proline stabilization mutations, as these can alter the conformational landscape of the pre-fusion S protein (Figure 1A; Data S1) (Gobeil et al., 2021a; Hsieh et al., 2020). We determined the structures of 3-RBD-down, 1-RBD-up, and 2-RBD-up populations of the Omicron and Delta S ectodomains (Figures 1, 2, and 3; Data S2 and S3). We observed considerable down-state variability in the Delta S1 subunit with one structural class presenting a disordered S1 subunit protomer, similar to an ectodomain structure we previously described in a mink-associated spike (Gobeil et al., 2021b). In contrast, the Omicron S protein displayed reduced S1 variability with several of its sixteen immune-evasive RBD amino acid substitutions stabilizing the RBD-RBD interfaces. These substitutions also stabilized 1-RBD-up states in a manner not observed in the Delta spike. The tight packing of the RBDs in the Omicron 3-RBD-down structures limits RBD motion. We observed a conformational rearrangement of the NTD-to-RBD (N2R) linker in a single protomer of an Omicron 3-RBD-down population, which was also identified in Delta and other variants but was comparatively rare among them. Altered S2 conformational dynamics were indicated by weaker binding of Omicron S protein (relative to the G614 and Delta S proteins) to 2G12 and other Fab-dimerized glycan-reactive (FDG) Abs that target a quaternary S2 glycan cluster, as well as by enhanced binding to FP-directed Ab DH1058. A high-resolution crystal structure of the FP-Ab complex suggests that enhancement must occur through release of the FP from its closed state position. Enhanced FP dynamics may therefore be linked to Omicron's enhanced transmissibility. Together, these results point to an Omicron spike that is evolved beyond immune evasion toward a more compact architecture with a well-regulated fusion machinery and altered dynamics of its FP that lead to more facile FP release.

RESULTS

Conformations of the SARS-CoV-2 Omicron S protein

As recent studies have reported structures of the Omicron S protein with proline stabilizing mutations in the S2 subunit (Cerutti et al., 2021; Ni et al., 2021; Cui et al., 2021; Zhou et al., 2021), either the 2P or the HexaPro mutations (Wrapp et al., 2020; Hsieh et al., 2020), we first assessed the effect of such stabilization by comparing binding of the S-GSAS-Omicron and S-GSAS-2P-Omicron with the ACE2 receptor ectodomain and RBD-directed Abs (Figures 1A and 1B). We found that CR3022, an Ab targeting a cryptic RBD epitope (Yuan et al., 2020), lost >90% binding to S-GSAS-2P-Omicron, suggesting that the 2P mutations are

limiting the conformational diversity of the Omicron S protein ectodomain. Reduced binding for the 2P versus non-2P Omicron spike is also seen for the 3-RBD-up conformation binding DH1047 and S2X259 Abs (Li et al., 2021; Tortorici et al., 2021). We therefore determined structures of the native Omicron S protein ectodomain in the S-GSAS form to examine the impacts the mutations had on its conformation (Figure 1; Table 1; Data S2). In the cryo-EM dataset, we identified 3-RBD-down, 1-RBD-up, and 2-RBD-up populations of the S protein ectodomain (Figure 1C). The Omicron spike harbors 16 amino acid substitutions in the RBD (Figure 1D), of which several have been shown to mediate ACE2 recognition and/or immune escape (Mannar et al., 2022; Cameroni et al., 2022). The 3-RBD-down populations were classified into two asymmetric reconstructions, with each displaying close RBD-RBD pairing. Of the two 3-RBD-down structures, named O1 and O2, the inter-protomer domain arrangement appeared more symmetric in O2 than in O1. This asymmetry was visualized in difference distance matrices (DDMs) that provide superposition-free comparisons between a pair of structures by calculating the differences between the distances of each pair of $C\alpha$ atoms in a structure and the corresponding pair of $C\alpha$ atoms in the second structure (Figure S2). In each reconstruction, we assigned the tag Protomer[1] to the protomer with the weakest RBD map density, which is suggestive of enhanced mobility (Figure 1C). Inter-protomer interactions between the "down" RBDs were mediated by a loop containing 3 amino acid substitutions, namely S371L, S373P, and S375F. A rearrangement of this RBD loop caused by the S373P mutation facilitated closer packing of the RBD-RBD interface via interactions of the region bearing the S373P and S375F substitutions in one protomer with the region bearing the N501Y and Y505H substitutions in the adjacent RBD (Figure 1E). In the 1-RBD-up structure, the S375F substitution created an inter-protomer interaction with residue F486 of the adjacent RBD-down protomer (Figure 1F). In the 2-RBD-up states, both up RBDs were disordered (Figure 1C). Overall, these results show that the mutations in the Omicron S protein induced coupling of the RBDs, causing unique S protein closed and open structural states.

We previously showed that the RBD-up/down transitions are accompanied by movements of the SD1/SD2 subdomains and of the N2R linker (residues 306–334) that connects the NTD and RBD within a single protomer unit (Figure 2A) (Gobeil et al., 2021a). In the RBD "down" state, the N2R region stacks against and contributes a β strand to each SD1 and SD2 subdomain (Figure 2B). Notably, in the Omicron 3-RBD-down O1 structure (PDB ID: 7TF8) (Figures 1C and 2B), we found that the N2R region secondary structures in the mobile Protomer[1] were

(B) Binding of S-GSAS-Omicron and S-GSAS-2P-Omicron to RBD-directed antibodies CR3022, S2X259 and DH1047, and to ACE2 receptor.
(C) Cryo-EM reconstructions of Omicron S protein 3-RBD-down (O1: EMDB: 25865, PDB 7TF8; O2: EMDB: 25983, PDB 7TL1), 1-RBD-up (O3: EMDB: 25846, PDB 7TEI; O4: EMDB: 25984, PDB 7TL9) and 2-RBD-up (O5: EMDB: 25880, PDB 7TGE; O6: EMDB: 26600) states, colored by protomer, and viewed down from the host-cell membrane. In the 1-RBD-up reconstructions, the "up" RBD is indicated by an asterisk (*). The black arrows in the 2-RBD-up reconstructions point to the "down" RBD.
(D) Omicron spike 3-RBD-down (O1: EMDB: 25865, PDB 7TF8) and 1-RBD-up (O3: EMDB: 25846, PDB 7TEI) structures, colored by promoter, and RBD mutations shown in red spheres.
(E and F) Inter-protomer RBD-RBD interactions in (E) the 3-RBD-down, and (F) the 1-RBD-up state.
See also Figures S1 and S2, Table 1, and Data S1 and S2.
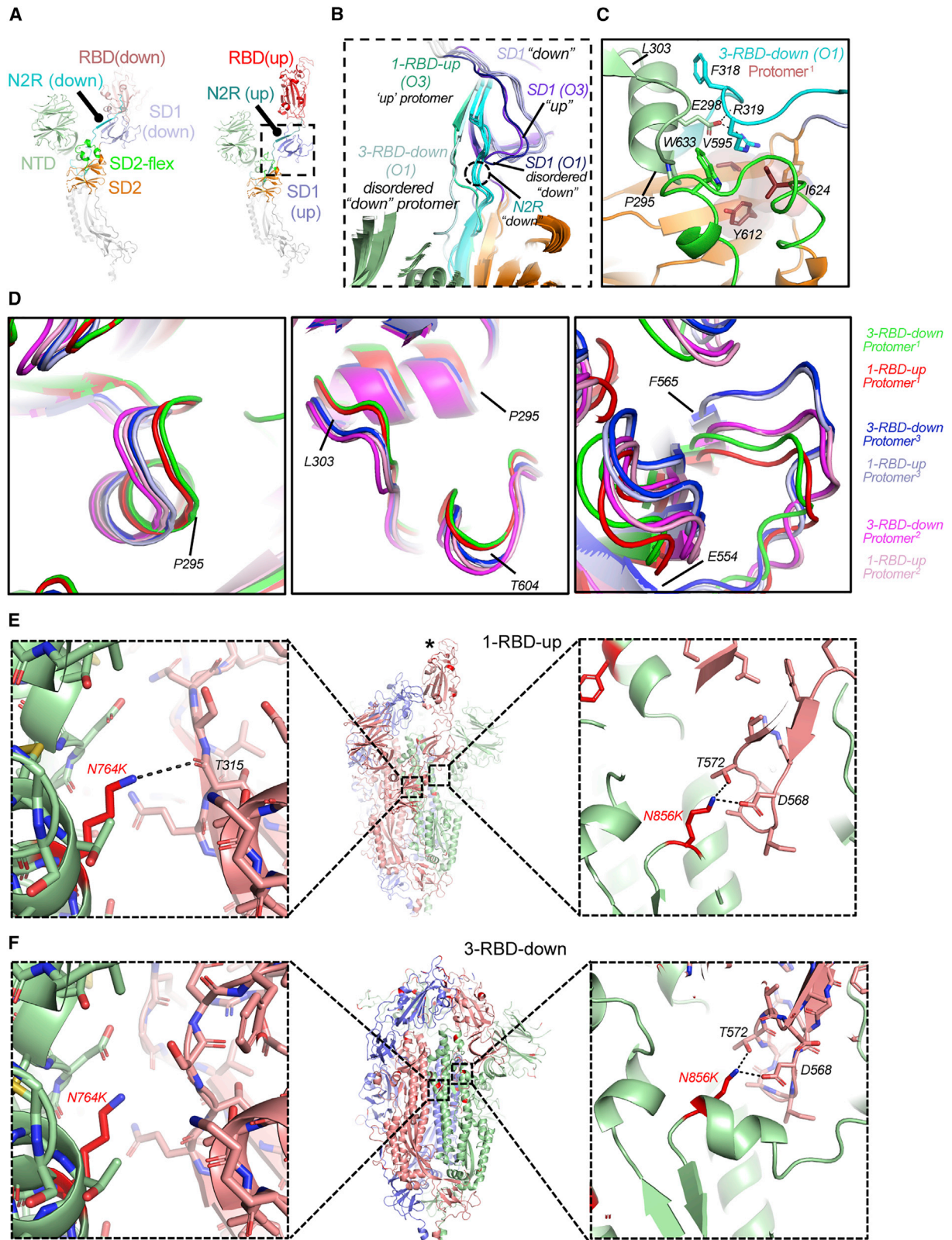
modified with a break in the SD2-associated β strand and were stabilized by a new intra-protomer salt bridge formed between R319 and NTD residue E298 (Figures 2B and 2C). This was accompanied by packing of residue F318 against the NTD 295–303 helix. This rearrangement permits interaction with a typically disordered segment of SD2, named "SD2-flex" here (residues 619–642). Stabilization of SD2-flex was facilitated by Van der Waals interactions of residue Ile624 (SD2-flex) with SD2 residues V595 and Y612 (Figure 2C) and by W633 packing between NTD residue P295 and N2R linker residue R319. The spatial positionings of the NTD helix 295–303, the SD2 loop, and the SD1 loop 554–565 were similar between the "up" protomer (Protomer[1]) of the 1-RBD-up structure and the mobile protomer (Protomer[1]) of the 3-RBD-down structure, suggesting that the mobile protomer may be poised to transition to the "up" position. The mobile SD1 region was stabilized in both the 3-RBD-down and 1-RBD-up Omicron S proteins via inter-protomer hydrogen bonding with the S2 subunit, mediated by residues D568 and T572 of SD1, with the N856K amino acid substitution near the Omicron S FP (Figures 2E and 2F). A hydrogen bond also formed between the carboxyl oxygen of residue T315 of the N2R linker in the "up" protomer, with the N764K substitution in the Omicron S protein. Thus, strategically placed residue substitutions in the Omicron S protein stabilize the highly mobile regions in the S1 subunit. Together, the close packing of the RBDs in the 3-RBD-down Omicron S protein and the N2R rearrangement in the "down" protomers define the wide range of conformational impacts that emanate from the extensive network of its acquired mutations.

Conformations of the SARS-CoV-2 Delta S protein

We next studied the Delta S protein to understand the differences in its structural properties that may underlie the differences in its pathobiology with Omicron. We determined cryo-EM structures of the S-GSAS-Delta S protein ectodomain (Figure 3; Table 2; Data S2). The Delta variant S protein includes two substitutions and a deletion in the NTD, two RBD substitutions, a P681R substitution proximal to the furin cleavage site, and a D950N substitution in the HR1 region of the S2 subunit (Figures 3A and S1). We identified 3-RBD-down (D1), 1-RBD-up (D2), and 2-RBD-up (D3) S protein ectodomain populations, as in the Omicron dataset, in addition to a population, named D4, which exhibited very high disorder in one of its S1 subunits

such that the entire S1 subunit, including the NTD, RBD, SD1, N2R linker, as well as part of the SD2 subdomain, were not visible in the cryo-EM reconstruction (Figure 3A). This was similar to a state found in a mink-associated spike (Gobeil et al., 2021b). The 3-RBD-down population was classified into six distinct subclasses (D5–D10) (Figure 3B), of which one (D6) displayed an N2R configuration observed in the Omicron O1 Protomer[1] (Figure 3C). A similar dislocation of the N2R region from its β-strand arrangement with the SD2 subdomain was also found in a "down" protomer of a 1-RBD-up subclass (D12) (Figure 3C), possibly representing an intermediate to the 2-RBD-up state. The array of distinct populations of the Delta S ectodomain that differ in their S1 subunit conformation are reminiscent of our observations with other naturally occurring variants (Gobeil et al., 2021a, 2021b), while the appearance of the single S1-protomer disordered state (Figures 3A and 3D) as we had observed in a mink-associated spike, hints of S protein instability originating in the mobile S1 region and encompassing the NTD, N2R linker, RBD, and SD1.

Domain positioning in Omicron, Delta, and engineered S proteins

We next investigated the source of the N2R linker rearrangements in the Delta and Omicron 3-RBD-down structures. The S1 subunit domain arrangements are responsive to one another across protomers through communication between adjacent, contacting RBDs, NTDs, and subdomains. We have demonstrated through engineering (Henderson et al., 2020) and by examination of previous variants (Gobeil et al., 2021a, 2021b) that this communication plays an essential role in RBD-up-/down-state presentation. The close interaction between RBDs in the Omicron spike led us to ask whether a design engineered to lock the 3-RBD-down state, termed rS2d for the introduced RBD to S2 disulfide staple, would show a similar N2R linker rearrangement due to restrictions on RBD movement. We obtained cryo-EM reconstructions of an S2 stabilized HexaPro version of the rS2d design (rS2d-HexaPro) and of the unstabilized rS2d (Figure 4; Table 3; Data S2) (Henderson et al., 2020; Hsieh et al., 2020; Edwards et al., 2021). Three-dimensional classification of both datasets led to two prominent structural states (Figure 4). One reconstruction in both datasets, each referred to as state 1, displayed a similar SD2 rearrangement as that observed in the Delta D6 and the Omicron O1 3-RBD-down

---

Figure 2. Intra-protomer communication through the NTD-to-RBD (N2R) linker

(A) Single protomers shown for RBD-down (left) and RBD-up (right) states, colored by domains: NTD – pale green, "up" RBD red, "down" RBD salmon, SD1 light and dark blue, respectively for the up and down protomer, N2R linker cyan for down protomer and deep teal for up protomer.

(B) Zoomed-in view of the N2R and surrounding regions showing overlay of all protomers. The N2R is colored sea green for the RBD-up protomer (Protomer[1]) in the 1-RBD-up structure O3, light cyan for the disordered RBD protomer (Protomer[1]) in the 3-RBD-down structure O1, and cyan for all the "down" RBD protomers (Protomer[2] and Protomer[3]). SD1 is colored lavender for all "down" protomers in O1 and O3 (Protomer[2] and Protomer[3]), purple and dark purple for Protomer[1] of O3 and O1, respectively.

(C) Zoomed-in view of the interaction of the N2R linker of Protomer[1] of the 3-RBD-down O1 state with the NTD helix spanning residue 295–303. N2R is colored cyan, NTD pale green, SD2 orange, and SD2-flex green. Brown surface shows interaction between V595, Y612, and I624.

(D) Overlay of protomers showing views of the NTD helix 295–303 (left), SD2 loop centered on T604 (middle) and SD1 region 554–565 (right). Protomers are colored as indicated. Superpositions were performed using S2 residues 908–1035.

(E) Stabilization of the SD1 and N2R regions in the "up" protomer of the 1-RBD-up structure via hydrogen bonds acquired through residue substitutions in the Omicron S protein.

(F) Stabilization of the SD1 region in the 3-RBD-down structure via hydrogen bonds acquired through residue substitutions in the Omicron S protein.

See also Figures S1 and S2, Table 1, and Data S1 and S2.
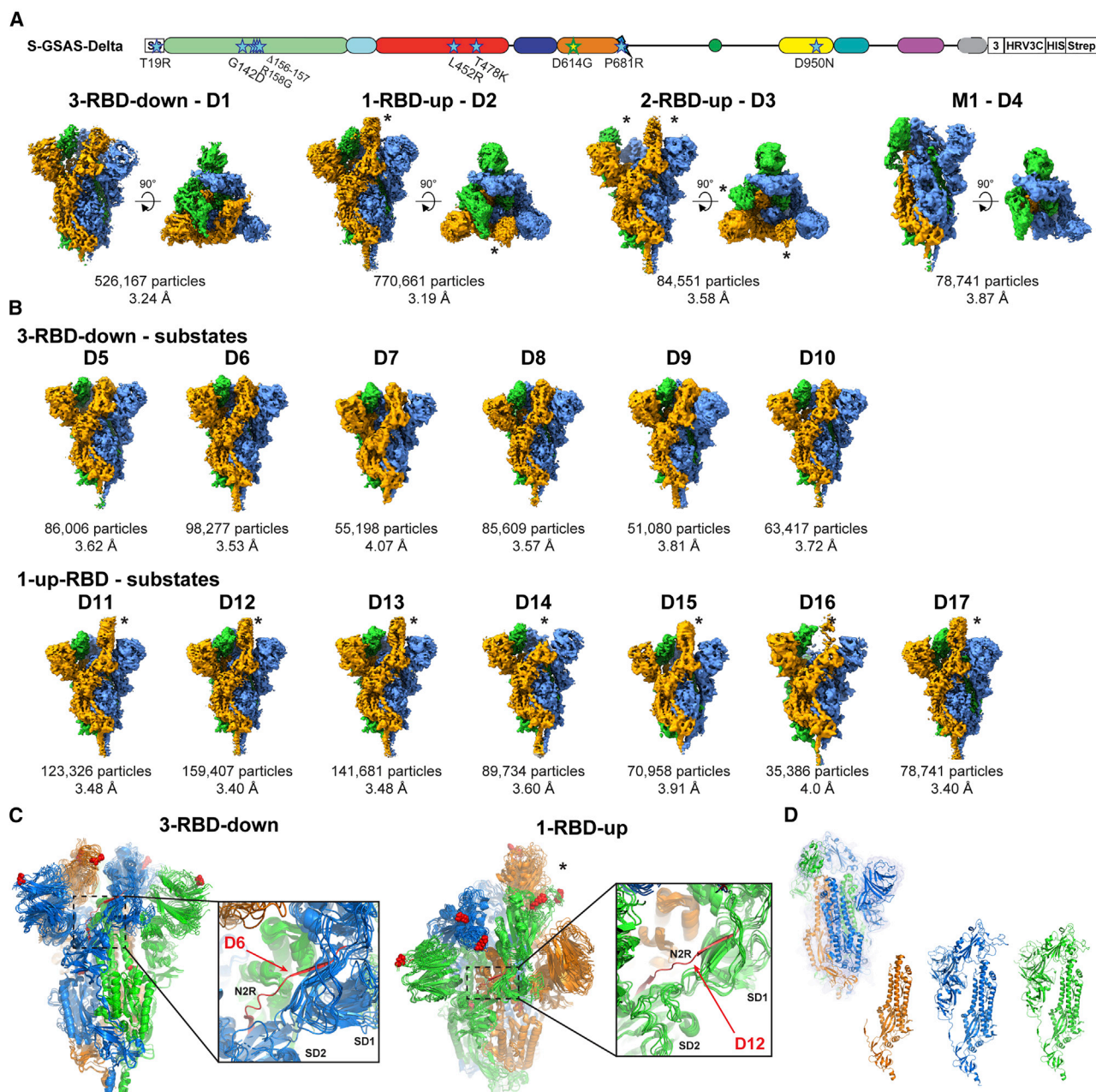
Figure 3. Conformational diversity of the SARS-CoV-2 Delta (B.1.617.2) S protein

(A) Top: domain architecture of the SARS-CoV-2 Delta S protomer. Bottom: side views and top views of the Delta S protein cryo-EM reconstructions of 3-RBD-down, 1-RBD-up, 2-RBD-up, and M1 states, colored by protomer. The "up" RBDs are indicated by an asterisk (*).

(B) Side views of subpopulations obtained by further classification of the states shown in (A).

(C) Left: overlay of 3-RBD-down subclasses. Dashed rectangle indicates the N2R region zoomed-in on the right image. The N2R linker in one of the Delta 3-RBD-down classes (D6) showed a N2R region that was dislodged from its beta strand arrangement with the SD2 subdomain and is shown in red. Right: overlay of 1-RBD-up subclasses. Dashed rectangle indicates the N2R region zoomed-in on the right image. The N2R linker in one of the two "down" protomers of a 1-RBD-up structure (D12) showed a N2R region that was dislodged from its beta strand arrangement with the SD2 subdomain and is shown in red. Mutations in the Delta variant are shown as red spheres.

(D) M1 state with the S1 subunit and SD2 subdomain of one of the three protomers disordered. The cryo-EM density is shown as a blue mesh with the underlying fitted model colored by protomer. The protomer colored orange shows disorder in the S1 subunit and SD2 subdomain; therefore, these regions could not be built in this protomer.

See also Figure S1, Table 2, and Data S1 and S3.

Table 1. Cryo-EM data collection and refinements statistics S-GSAS-Omicron, related to Figures 1 and 2

	3-down		1-up		2-up	
PDB ID	7TF8	7TL1	7TEI	7TL9	7TGE	
EMDB ID	25865	25983	25846	25984	25880	26600
Data collection and processing						
Microscope	FEI Titan Krios					
Detector	Gatan K3					
Magnification	81,000					
Voltage (kV)	300					
Electron exposure (e⁻/Å²)	60					
Defocus range (μm)	2.2–0.7					
Pixel size (Å)	1.08					
Reconstruction software	cryoSPARC					
Symmetry imposed	C1	C1	C1	C1	C1	C1
Initial particle images (no.)	7,059,633					
Final particle images (no.)	387,017	194,909	328,521	159,915	215,168	101,363
Map resolution (Å)	3.4	3.5	3.4	3.5	3.7	4.0
FSC threshold	0.143	0.143	0.143	0.143	0.143	0.143
Coordinate refinement						
Initial model used	7KDK	7TF8	7KDL, 7B3O	7TEI	7TEI	–
Model composition						
Nonhydrogen atoms	25,732	25,109	25,420	25,016	21,461	–
Protein residues	3,153	3,138	3,044	3,083	2,677	–
R.M.S. deviations						
Bond lengths (Å)	0.004	0.003	0.004	0.004	0.004	–
Bond angles (°)	0.698	0.664	0.657	0.703	0.734	–
Validation						
MolProbity score	1.28	1.35	1.29	1.42	1.39	–
Clashscore	2.77	3.26	2.65	3.58	3.48	–
Poor rotamers (%)	0.07	0	0	0	0.13	–
EM ringer score	2.93	2.56	2.83	2.56	0.89	–
Ramachandran plot						
Favored (%)	96.6	96.45	96.46	96.08	96.22	–
Allowed (%)	3.4	3.55	3.54	3.92	3.78	–
Disallowed (%)	0	0	0	0	0	–

structures (Figure 4A). Examination of a structural morph between both states (Video S1) identified a marked shift in the SD1 toward SD2 in the linker-displaced protomer (Figures 4B and 4C). Because of the proximity between the two subdomains, the β-sheet secondary structure linking the two was broken, which in turn broke the paired N2R β-sheet structure (Figure 4B). The loss of this secondary structure permits the observed rearrangement in the linkers and the disordered segment.

We next asked whether the features in the rS2d spike domain arrangements that led to N2R linker rearrangement occurred in the Delta and Omicron 3-RBD-down states. Alignment of the SD2 subdomains of the N2R-rearranged protomers indicated that the overall subdomain and NTD domain arrangements were similar, except for the state 2 protomers (Figure 4D). Alignment of the disordered RBD (Protomer[1]) revealed that the RBD positions differed markedly among the trimers (Figure 4D).

Using a vector-based quantification of S protein domain arrangement (Henderson et al., 2020; Gobeil et al., 2021b), we previously found that absolute positions in spike domains may differ but that trends in their overall architecture are correlated with important structural features such as the propensity to occupy the RBD-up state. The most important feature observed in the SD2-rearranged rS2d state was forcing of the SD1 toward its adjacent SD2.

We examined a series of vectors connecting the subdomains and NTDs of each protomer (Figure 5A) and found that while the angle and distance values differed slightly, the trend in relative positions was the same for each of the S protein trimers where the N2R rearrangement was observed (Figure 4E). Specifically, the shift in SD1 position toward SD2 relative to the rS2d and rS2d-HexaPro state 2 was retained, consistent with a role of these subdomain shifts in causing the N2R rearranged state.

Table 2. Cryo-EM data collection and refinements statistics S-GSAS-Delta, related to Figure 3

	D1	D5	D6	D7	D8	D9	D10	D2	D11	D12	D13	D14	D15	D16	D17	D3	D4
		S-GSAS-Delta															
	3-down consensus	3-down						1-up consensus	1-up							2up	M1
PDB ID	7TOU	7TOX	7TOY	7TOZ	7TP0	7TP1	7TP2	7TOV	7TP7	7TP8	7TP9	7TPA	7TPC	7TPE	7TPF	7TPH	7TPL
EMDB ID	26038	26040	26041	26042	26043	26045	26046	26039	26047	26048	26049	26050	26051	26052	26053	26055	26059
Data collection and processing																	
Microscope	FEI Titan Krios																
Detector	Gatan K3																
Magnification	81,000																
Voltage (kV)	300																
Electron exposure (e^-/Å^2)	55																
Defocus range (μm)	−0.75 to 2.5																
Pixel size (Å)	1.08																
Reconstruction software	CryoSparc																
Symmetry imposed	C1																
Initial particle images (no.)	2,698,323																
Final particle images (no.)	526,167	86,006	98,277	55,198	85,609	51,080	63,417	770,661	123,326	159,407	141,681	89,734	70,958	35,386	155,352	84,551	78,741
Map resolution (Å)	3.24	3.62	3.53	4.07	3.57	3.81	3.72	3.16	3.48	3.4	3.48	3.6	3.91	4	3.4	3.58	3.87
FSC threshold	0.143	0.143	0.143	0.143	0.143	0.143	0.143	0.143	0.143	0.143	0.143	0.143	0.143	0.143	0.143	0.143	0.143
Coordinate refinement																	
Initial model used	7KDK							7KDL								7KDL	7KDL
Model composition																	
Nonhydrogen atoms	24,687	24,618	24,673	24,470	24,589	24,646	24,663	23,199	23,199	23,199	23,199	23,199	23,199	23,199	23,199	22,180	19,992
Protein residues	3,050	3,041	3,049	3,026	3,040	3,046	3,047	2,983	2,983	2,983	2,983	2,983	2,983	2,983	2,983	2,912	2,485
R.M.S. deviations																	
Bond lengths (Å)	0.013	0.013	0.013	0.013	0.013	0.013	0.013	0.013	0.013	0.013	0.013	0.013	0.013	0.013	0.013	0.013	0.013
Bond angles (°)	1.809	1.746	1.765	1.825	1.747	1.741	1.754	1.794	1.756	1.754	1.756	1.745	1.826	1.733	1.747	1.748	1.785
Validation																	
MolProbity score	1.07	1.11	1.12	1.60	1.22	1.15	1.13	0.94	1.08	0.97	0.98	0.99	1.46	1.32	0.94	1.03	1.39
Clashscore	0.16	0.12	0.08	0.64	0.27	0.16	0.18	0.07	0.13	0.04	0.02	0.00	0.42	0.20	0.04	0.14	0.35
Poor rotamers (%)	1.2	1.35	1.50	2.87	1.62	1.39	1.32	0.89	1.15	0.98	0.94	1.11	2.26	1.83	0.72	1.01	1.94
EM ringer score	3.52	2.42	2.97	0.33	2.66	1.81	2.45	4.13	3.20	4.23	3.41	2.96	0.71	1.78	3.82	3.36	2.53

(*Continued on next page*)

Table 2. Continued

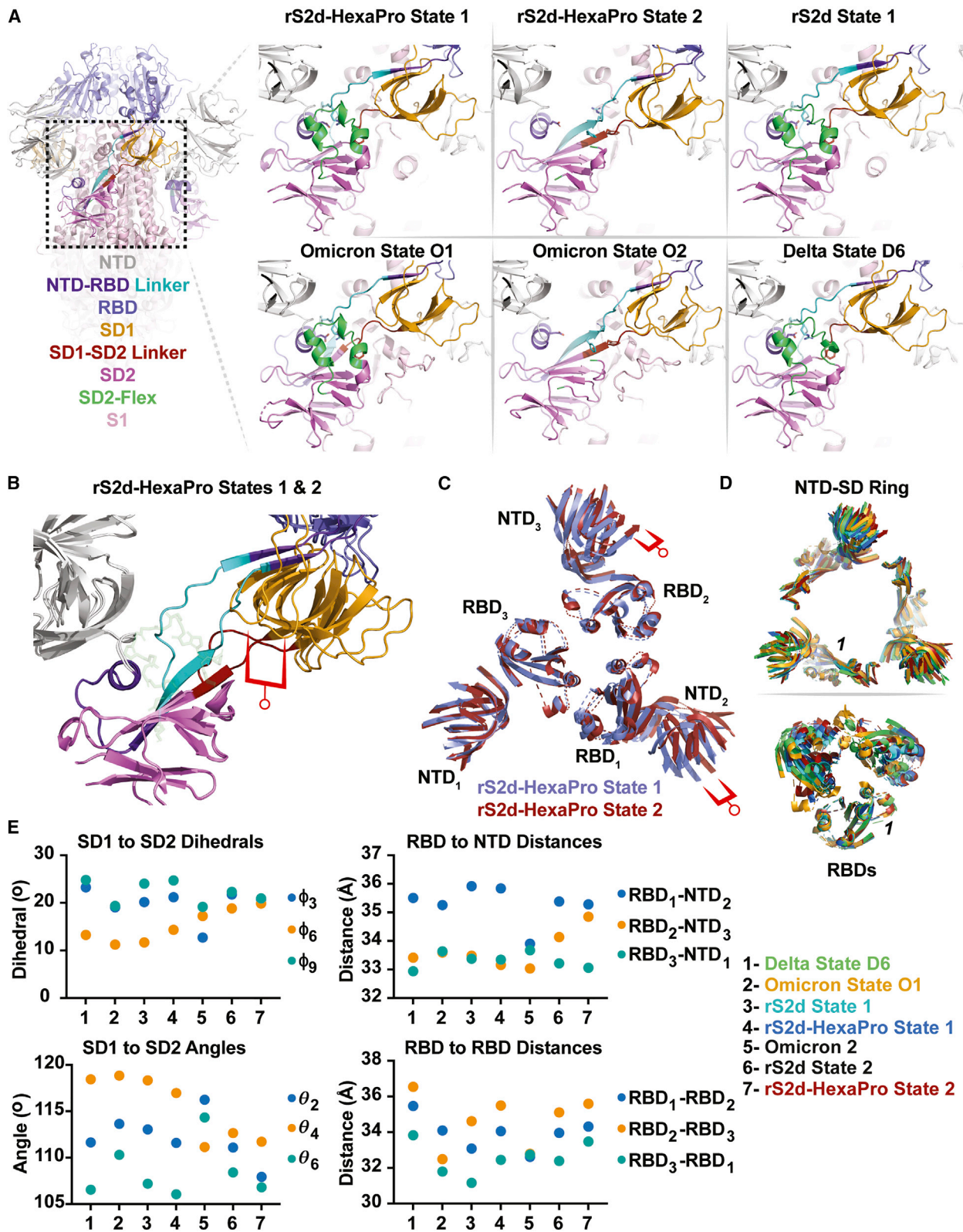|	D1	D5	D6	D7	D8	D9	D10	D2	D11	D12	D13	D14	D15	D16	D17	D3	D4
		S-GSAS-Delta														2up	M1
	3-down consensus	3-down						1-up consensus	1-up								
Ramachandran plot																	
Favored (%)	93.18	92.78	92.81	90.42	92.59	92.40	92.43	93.74	92.26	92.81	92.40	92.78	90.14	90.31	93.53	92.27	90.38
Allowed (%)	6.16	6.68	6.76	8.74	6.65	6.73	7.17	5.82	7.05	6.26	6.88	6.47	8.83	8.59	6.13	7.16	8.6
Disallowed (%)	0.67	0.53	0.43	0.84	0.77	0.87	0.40	0.45	0.68	0.92	0.72	0.75	1.03	1.10	0.34	0.56	1.1

These local effects were accompanied by a reduced distance between the RBD-NTD pair across from the disordered RBD protomer (RBD_2 to NTD_3) suggesting that despite variability in RBD positions, this interaction plays a role in the N2R rearrangement (Figure 4E). Though the N2R rearranged trimers were similar, the non-rearranged state 2 trimers of the Omicron and rS2d trimers differed markedly. Together, comparison of the rS2d constructs and the variant structures indicates that local and global rearrangements in S1 lead to the rearranged state.

Vector analysis of intra- and inter-protomer domain relationships in the Omicron and Delta S proteins

We next examined clustering of the Omicron and Delta variant 3-RBD-down structures with previous variant structures utilizing sets of inter-protomer and intra-protomer vectors using principal components analysis (PCA) (Figure 5A). As suggested by visual inspection of the Omicron variant structures, the Omicron trimers formed a distinct cluster in PCA of the inter-protomer vector set (Figure 5B). The Delta structures were spread throughout the variant structure set along principal component one, consistent with the structural variability recovered through sub classification of the cryo-EM dataset (Figure 3). These results demonstrate the considerable structural rearrangements that the S protein has acquired through SARS-CoV-2 evolution (Figure 5B). The structural conservation of the rearranged N2R state between the engineered and variant S proteins suggests that this plays a specific role in S1 dynamics. As a specific domain organization accompanies the appearance of this state, we asked whether previous variant structures may present this state, albeit at lower proportions of the total population and with less conspicuous map density. We therefore examined the intra-protomer vector set by PCA to identify candidate structures (Figures 5A and 5C). Consistent with the inter-protomer vectors, N2R rearranged protomers of the rS2d constructs, and the Omicron and Delta variants occupied a distinct position along principal component one (Figure 5C). Protomers from the D614G, Mink, and Beta variants clustered with these structures. Densities in the N2R region for these structures were consistent with the rearranged state as determined by fitting of the rS2d state 1 coordinates, where this N2R rearranged state was particularly well resolved, to the respective cryo-EM densities (Figure 5D). As expected, the densities were less clear than in the rS2d constructs, suggestive of multistate or dynamic behavior. As was observed in the rS2d, Omicron, and Delta structures, the rearranged N2R protomer contained the disordered RBD and corresponded to the most distant RBD-NTD pair. These results highlight the differences in the Omicron 3-RBD-down structures from other variant S proteins, characterized by the stabilization of a N2R rearranged state.

Antigenicity of the Omicron and Delta S proteins

We next studied the antigenicity and receptor-binding properties of the Omicron S protein. Consistent with the extensive immune escape observed with the Omicron variant (Cameroni et al., 2022; Planas et al., 2022; Mannar et al., 2022; Hoffmann et al., 2022; Schmidt et al., 2022), we found that its S protein lost binding to several SARS-CoV-2 neutralizing Abs (Figures 6A–6C and S3). Ab DH1050.1 that targets a site of vulnerability in

A

rS2d-HexaPro State 1   rS2d-HexaPro State 2   rS2d State 1

Omicron State O1   Omicron State O2   Delta State D6

NTD
NTD-RBD Linker
RBD
SD1
SD1-SD2 Linker
SD2
SD2-Flex
S1

B   rS2d-HexaPro States 1 & 2

C

NTD$_3$

RBD$_3$ RBD$_2$

NTD$_1$ RBD$_1$ NTD$_2$

rS2d-HexaPro State 1
rS2d-HexaPro State 2

D   NTD-SD Ring

1

RBDs

1

E

SD1 to SD2 Dihedrals

ϕ_3
ϕ_6
ϕ_9

RBD to NTD Distances

RBD$_1$-NTD$_2$
RBD$_2$-NTD$_3$
RBD$_3$-NTD$_1$

SD1 to SD2 Angles

θ_2
θ_4
θ_6

RBD to RBD Distances

RBD$_1$-RBD$_2$
RBD$_2$-RBD$_3$
RBD$_3$-RBD$_1$

1- Delta State D6
2- Omicron State O1
3- rS2d State 1
4- rS2d-HexaPro State 1
5- Omicron 2
6- rS2d State 2
7- rS2d-HexaPro State 2

(legend on next page)

the NTD (McCallum et al., 2021b; Li et al., 2021) no longer bound the Delta and Omicron S proteins (Figures 6A and 6B). The non-neutralizing and protective Ab DH1052 retained binding to the Delta but not to the Omicron S protein, with its binding likely disrupted by changes in the region spanning residues 211–215 of the Omicron S protein (Figures 6A and 6B) (Li et al., 2021). The RBD receptor-binding-site-directed Abs DH1041 and DH1042 lost binding to Omicron S protein while DH1042 also lost binding to Delta S protein. Both Omicron and Delta S proteins retained similar binding levels to ACE2 (Figures 6A, 6C, and S3). DH1041 and DH1042 bound similar RBD epitopes overlapping the ACE2 binding site (Figures 6C and S4; Table 4; Data S5) (Li et al., 2021), showing that subtle changes in epitope footprint can alter the susceptibility profile of Abs to residue substitutions. For DH1042, insertion of a charged residue within a hydrophobic binding site by the L452R substitution in the Delta S protein (Figure S4) resulted in reduction of binding and loss in neutralization activity. Indeed, DH1042 showed substantially reduced binding to S-GSAS-L452R and the S-GSAS-Epsilon S protein ectodomain (B.1.429) that harbors the L452R substitution. DH1041 binding, on the other hand, was unaffected by the L452R substitution (Figure S4).

Consistent with its reported retention of Omicron neutralization, albeit at reduced levels, Ab S309 (Pinto et al., 2020), the parental form of the engineered therapeutic Ab Sotrovimab, retained substantial binding to the Omicron spike (Figures 6A and S3). The broad sarbecovirus neutralizing Ab DH1047 (Li et al., 2021; Martinez et al., 2022) lost substantial binding to the Omicron spike, resulting in loss in its neutralization activity against Omicron (Cao et al., 2022). The S2X259 Ab targets a similar epitope (Tortorici et al., 2021) but retained binding and neutralization activity against Omicron (Cameroni et al., 2022). The SARS-CoV-2 cross-reactive Ab CR3022 targeted a cryptic, unmutated epitope on the spike and retained binding to the S-GSAS-Omicron and Delta spikes despite considerable differences in their S1 subunit dynamics. Two RBD-directed Abs, DH1044 and DH1193, that do not compete for ACE2 binding (Li et al., 2021) retained binding to the Omicron S protein. The DH1044 epitope was mapped by NSEM to a region adjacent to the epitope of Ab S309, although shifted toward residue L452, making it susceptible to the L452R substitution in the Delta spike (Figures 6A and 6C) (Li et al., 2021). Mapping of the DH1193 epitope by NSEM revealed an epitope in between the S309 and DH1044 epitopes (Figure S5). Consistent with their binding to the Omicron S protein, Abs DH1044 and DH1193 neutralized

SARS-CoV-2 D614G and Omicron in a pseudovirus neutralization assay (Data S6).

We next probed S2 subunit conformation by measuring binding to S2 targeting Abs (Figures 6D, 7A, S3, S6, and S7). We have previously described the binding of HIV-1 neutralizing, FDG Ab 2G12 to a quaternary glycan cluster in the S2 subunit of the SARS-CoV-2 S protein (Williams et al., 2021) and have demonstrated that 2G12 binding is sensitive to changes in S protein conformation (Edwards et al., 2021; Gobeil et al., 2021b). 2G12 and a panel of FDG Abs targeting the same glycan cluster (Williams et al., 2021) showed glycan-dependent binding to the Delta and Omicron S proteins (Figures 6D and S7). Binding of 2G12 to the Omicron S protein was weaker than its binding to the G614 and Delta S proteins, suggesting altered presentation of the glycan cluster either due to a global change in S2 conformation or a local change due to the stabilization of glycan 709 by the D796Y substitution resulting in a change in presentation of the glycan epitope (Figure 6D). These results are consistent with considerable Omicron S protein structural shifts and suggest that S2 dynamics and flexibility are impacted by its acquired mutations.

Altered FP dynamics in the Omicron S protein

We next tested binding by ELISA of the G614, Delta, and Omicron spikes to SARS-CoV-2 FP-directed Ab DH1058 (Figure 7A) (Li et al., 2021). DH1058 binds a 25-residue peptide spanning residues 808–833 that includes the FP (Gobeil et al., 2021b) and showed ~6-fold increased binding to S-GSAS-Omicron compared with the G614 and Delta S proteins, suggesting greater access of DH1058 to the FP in the Omicron S protein (Figure 7A). S-GSAS-2P-Omicron binding to DH1058 was substantially reduced compared with S-GSAS-Omicron, suggesting reduced accessibility of the FP epitope when the 2P mutations were incorporated in the Omicron S protein. Binding rate and equilibrium constants (k_{on}, k_{off}, and K_D) measured by SPR revealed no differences between S-GSAS-Omicron and the corresponding D614G and Delta S protein constructs (Figure 7B). As the ELISA assay measures binding on a timescale slower than that captured by the SPR assay, these results suggested time-dependent changes in the accessibility or presentation of the DH1058 epitope, as the Ab is incubated with the spike for longer times in an ELISA experiment. The FP residues that are targeted by DH1058 were well resolved in the cryo-EM reconstruction of the Omicron S protein (Figure 7C) with more residues resolved in the cryo-EM reconstruction compared with other variant

Figure 4. The down-state locked rS2d trimer is structurally similar to the Omicron 3-RBD-down S protein
(A) (Left) Spike trimer ectodomain highlighting the SD2 region. (Right) Structural states of the rS2d, rS2d-HexaPro, Omicron, and Delta state D6 Spikes in the region of SD2 highlighting structural rearrangements in the linking regions (cyan and dark red) and flexible SD2 segment (green).
(B) Comparison of the SD1 with SD2 disposition between rS2d-HexaPro states 1 and 2 via alignment of the SD2 core residues. The red indicator highlights the distance shift in SD1.
(C) NTD aligned RBD pairings between rS2d-HexaPro states 1 and 2. The red indicator highlights the difference in RBD disposition relative to the NTD in the RBD2 to NTD3 pairing. Only sheet and helix elements are shown for clarity.
(D) (Top) Alignment of the NTDs and subdomains of the rS2d-HexaPro states 1 and 2, rS2d state 1, Omicron, and Delta D6 trimers. (Bottom) Alignment of the rS2d-HexaPro states 1 and 2, rS2d state 1, Omicron O1, and Delta D6 trimer RBDs. Only sheet and helix elements are shown for clarity. Number indicates protomer 1 position.
(E) Vector dihedral, angle, and distances defining differences and similarities between the rS2d-HexaPro states 1 and 2, rS2d states 1 and 2, Omicron O1, and Delta D6 trimers. Phi angles 3, 6, and 9 and Theta angles 2, 4, and 6 correspond to dihedrals/angles in protomers 3, 1, and 2, respectively.
See also Data S4 and Table 3.

Table 3. Cryo-EM data collection and refinements statistics rS2d, related to Figure 4

	rS2d State 1	rS2d State 2	rS2d-HexaPro State 1	rS2d-HexaPro State 2
	rS2d and rS2d-HexaPro Structures			
	3-down			
PDB ID	7TLA	7TLB	7TLC	7TLD
EMDB ID	EMD-25985	EMD-25986	EMD-25987	EMD-25988
Data collection and processing				
Microscope	Titan Krios			
Detector	Gatan K3			
Magnification	81,000			
Voltage (kV)	300			
Electron exposure ($e^-/Å^2$)	65.81		53.13	
Defocus range (μm)	−0.8 to 2.5		−0.8 to 2.5	
Pixel size (Å)	1.06		1.058	
Reconstruction software	cryoSPARC			
Symmetry imposed	C1			
Initial particle images (no.)	5,115,041		1,287,203	
Final particle images (no.)	149,387	218,600	398,297	275,353
Map resolution (Å)	3.13	3.06	2.83	2.89
FSC threshold	0.143			
Coordinate refinement				
Initial model used	6X29			
Model composition				
Nonhydrogen atoms	23,052	22,806	23,052	22,806
Protein residues	2,948	2,916	2,948	2,916
R.M.S. deviations				
Bond lengths (Å)	0.012	0.012	0.012	0.012
Bond angles (°)	1.854	1.839	1.909	1.887
Validation				
MolProbity score	1.04	0.91	1.06	0.90
Clashscore	0.09	0.11	0.04	0.04
Poor rotamers (%)	1.32	0.86	1.59	0.94
EM ringer score	4.03	3.68	4.03	3.69
Ramachandran plot				
Favored (%)	93.68	94.66	94.30	94.48
Allowed (%)	6.01	5.27	5.42	5.38
Disallowed (%)	0.31	0.07	0.28	0.14

S proteins. The overall orientation of the FP was conserved between D614G, Alpha, Beta, Delta, and Omicron S protein structures (Figure 7C). While several attempts to obtain cryo-EM structures of DH1058 bound to furin-cleaved and uncleaved spikes were unsuccessful, we obtained a crystal structure of DH1058 Fab bound to a peptide comprising FP residues 808–833 at a resolution of 2.15 Å (P 1 2$_1$ 1 space group) (Figure 7D; Table 5). The interaction between DH1058 and the FP is mediated by all heavy chain (HC) complementary determining regions (CDRs). The portion of the FP between residues 816 and 825 defines the interaction with Ser816 and Asp820 sidechains forming hydrogen bonds (H-bond) with the HCDR2 residues Y53, E54, R56, and N57 side chains. The HCDR1 D31 main chain

carbonyl formed an H-bond with the FP R815 sidechain, while the HCDR3 Y115 and Y116 formed sidechain-to-sidechain H-bonds with E819 and K825, respectively (Figure 7D). Aligning the structure of the trimeric pre-fusion Omicron S protein using the FP fragment from the crystal structure for superposition revealed clashes between the SD2 subdomain and bound DH1058 HC loops 13–17, 61–68, and 84–88, and the S2 subunit HR1 subdomain and DH1058 HCDR2 (Figure 7E). These data show that the binding of DH1058 to the SARS-CoV-2 FP, as revealed by the crystal structure, is incompatible with the structures of the pre-fusion SARS-CoV-2 S proteins. Taken together, these data suggest that a weak initial contact of the DH1058 with the FP is made in the pre-fusion S protein ectodomains as
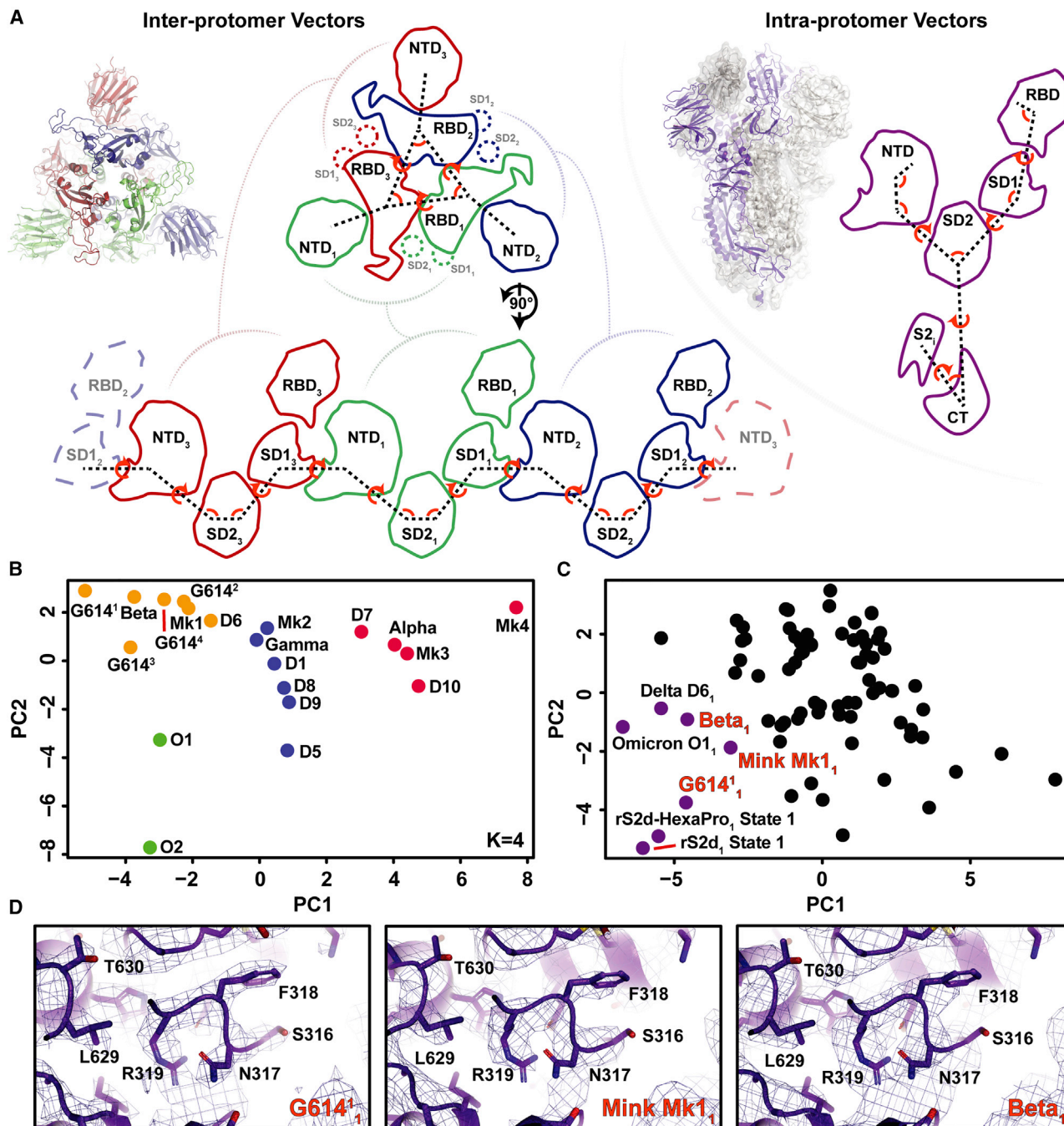
Figure 5. Intra- and inter-protomer domain relationships in SARS-CoV-2 3-RBD-down S proteins

(A) (Left) Inter-protomer vectors describing the relationship between the NTDs, RBDs, and subdomains across protomers. (Right) Intra-protomer vectors describing domain geometries within a protomer.

(B) Principal components analysis of the inter-protomer vectors for each variant structure. Colors indicate K-means centers using a total of four centers. The M notation indicates values from previously determined structures of the cluster-5, mink-associated spike (PDB IDs 7LWL, 7LWI, 7LWK, 7LWJ for M1-4, respectively), while the G614 superscript notation indicates values from previously determined structures for the D614G spike (PDB IDs 7KE8, 7KE6, 7KE7, and 7KE4 for G614[1–4], respectively).

(C) Principal components analysis of the intra-protomer vectors for each variant structure protomer. Protomers displaying the N2R rearrangement are highlighted in purple.

(D) Previously determined cryo-EM maps of the principal components analysis identified N2R rearranged protomers aligned with the state 1 rS2d N2R rearranged protomer.

See also Video S1.
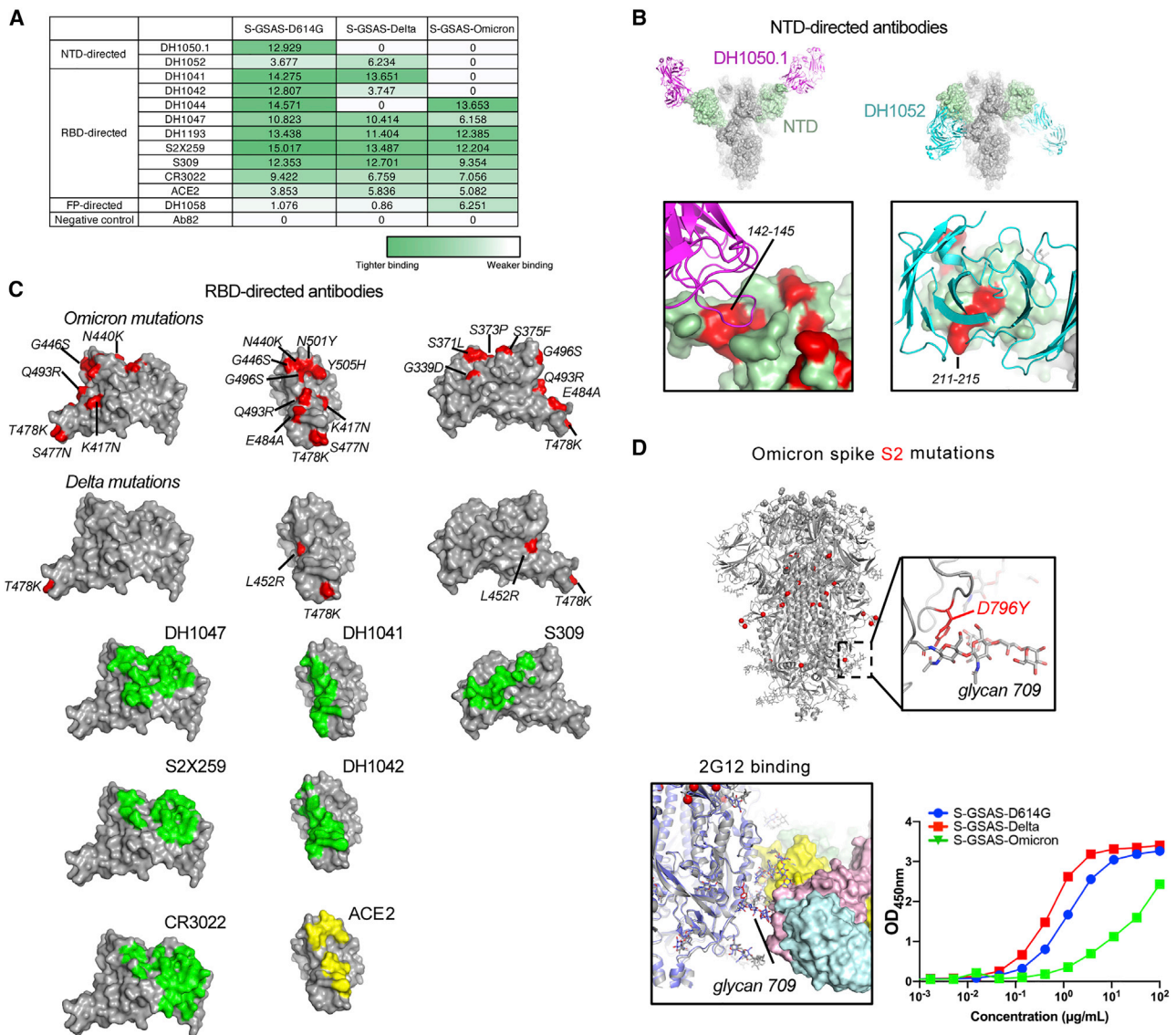
Figure 6. Impact of Delta and Omicron mutations on the antigenicity of the SARS-CoV-2 S protein

(A) Antibody binding to SARS-CoV-2 S proteins measured by ELISA. The binding values were obtained by calculating area under curve of ELISA binding curves.

(B) Binding of NTD directed antibodies DH1050.1 and DH1052 to the SARS-CoV-2 spike.

(C) Top two rows show three views of the RBD with residues mutated in Omicron (top row) and Delta (second row) colored red. Binding sites of RBD-directed antibodies and ACE2 receptor to SARS-CoV-2 S ectodomains are shown.

(D) Top: Omicron 3-RBD-down spike is shown in gray, with residue changes relative to the D614G variant shown as spheres. Residue changes in the S2 region are colored red. The zoomed-in image shows glycan 709 and its interaction with the D796Y substitution. Bottom: binding of 2G12 to SARS-CoV-2 S proteins. See also Figures S3–S7 and Table 4.

captured in the SPR assay, followed by a conformational change in the spike leading to greater FP exposure and stable binding of the DH1058 Fab. DH1058 Fab cannot bind stably to the pre-fusion conformation of the SARS-CoV-2 S protein, consistent with its lack of SARS-CoV-2 neutralization activity (Li et al., 2021) and would require greater exposure of the FP to make a stable interaction, avoiding clashes with adjacent regions of the pre-fusion S protein. Our data here suggest that the conformational changes leading to greater FP exposure occur more readily in the Omicron S protein. Taken together, these

results show altered flexibility and ease of exposure and release around the FP region in the S2 subunit of the Omicron spike relative to other variants.

DISCUSSION

As SARS-CoV-2 continues to evolve, the emergence of the Omicron variant is poised to change the course of the COVID-19 pandemic with its unprecedented transmissibility and immune evasion. The Omicron spike protein, which is central

**Table 4. Cryo-EM data collection and refinements statistics DH1042 Fab, related to Figure 6**

	SARS-CoV-2 S−2P + DH1042 Fab	SARS-CoV-2 RBD + DH1042 Fab
PDB ID	7THT	7THE
EMDB ID	EMD-25904	EMD-25893
Microscope	Titan Krios	
Detector	Gatan K3	
Magnification	81,000	
Voltage (kV)	300	
Electron exposure (e⁻/Å²)	54.02	
Defocus range (μm)	−0.7.5 to 2.5	
Pixel size (Å)	1.058	
Reconstruction software	cryoSPARC	
Symmetry imposed	C1	
Initial particle images (no.)	6,802,454	
Final particle images (no.)	175,460	78,958
Map resolution (Å)	3.42	3.87
FSC threshold	0.143	
Refinement		
Model composition		
Nonhydrogen atoms	28,905	3,305
Protein residues	3,651	423
R.M.S. deviations		
Bond lengths (Å)	0.013	0.013
Bond angles (°)	1.868	1.880
Validation		
MolProbity score	2.19	1.11
Clashscore	6.88	0.31
Favored rotamers (%)	97.07	94.46
EM ringer score	3.22	3.24
Ramachandran plot		
Favored (%)	92.90	91.85
Allowed (%)	6.59	8.15
Disallowed (%)	0.50	0.00

to defining these properties, is riddled with mutations in both its receptor-binding S1 subunit and its fusion subunit S2. As the exposure of Ab and receptor-binding sites can be affected by both direct substitutions at the binding interface and conformational masking of key sites, we have sought here to understand the conformational changes of the Omicron spike resulting from its altered primary sequence. Our structural studies were performed in our previously established platform S-GSAS that did not contain any extraneous stabilizing mutations in the S2 subunit, thus aiming to visualize S protein conformations in a more native format (Gobeil et al., 2021a, 2021b). Indeed, we were able to resolve a more varied repertoire of structural states of the Omicron S protein than were revealed by several studies that have used constructs with stabilizing proline mutations in the S2 subunit (Zhou et al., 2021; Cerutti et al., 2021; Ni et al.,

2021; Cui et al., 2021). The Omicron S protein presented a substantially different domain organization compared with other variants (Figure 1)—differences that we were able to visualize in our structures and quantify using sets of intra- and inter-protomer vectors (Figures 1, 4, and 5). We found a tightly packed RBD-RBD interface in the 3-RBD-down state, with new inter-protomer interactions mediated by a RBD loop harboring the S371L, S373P, and S375F substitutions in one protomer and a Y505H substitution in the adjacent interacting protomer. The close packing of the down-state RBDs in Omicron is distinct from how the previous VOCs have evolved. While previous VOCs maximized transmissibility by favoring open states of the spike and immune evasion by mutating common Ab epitopes, acquisition of RBD-down state stabilizing mutations is a significant change in a different direction. The observed stabilization of the RBD-down state in the Omicron S protein may contribute to immune evasion by occluding highly immunogenic sites that bind very potent Abs. Moreover, the Omicron variant is more transmissible than any variant isolated so far. How does the Omicron spike achieve high transmissibility, which would require open states of the spike to engage receptor and undergo fusion, while also bolstering RBD-down-state stability? The answer to this lies potentially in two aspects of our structural analysis. First, we showed structural evidence that the stabilization of a 3-RBD-down state of the Omicron spike accompanied rearrangements in the critical N2R linker that connects the NTD and RBD in a protomer, such that one protomer in the 3-RBD-down spike is primed to transition to the up-state. Thus, the stabilization of the 3-RBD-down state is balanced by an enhanced propensity to adopt the up-state due to rearrangements in the N2R linker. Second, by combining binding assays, X-ray crystallography, and cryo-EM, we uncovered evidence for altered plasticity of the FP in the Omicron spike compared with other variants, including Delta. Despite extensive stabilization of the Omicron spike, the functionally critical FP is more easily exposed in Omicron as measured by binding to a fusion peptide-directed Ab. Thus, the increased transmissibility of the Omicron spike may be facilitated by a combined effect of the ease of accessing the RBD-up state despite stabilization of the down-state RBD-RBD interface, retained affinity for ACE2 interactions despite the large number of RBD mutations, as well as by more ready release of the FP. Further functional studies will be needed to determine the extent to which the structural observations reported here impact the biological properties of the Omicron variant. Close monitoring of the continued evolution of the structure of future variants on the Omicron template will be required to achieve a deep understanding of Omicron pathobiology and to anticipate the immune escape potential of the further evolved variants.

Limitations of the study

The data reported in this study have been obtained using an engineered SARS-CoV-2 spike ectodomain construct where the furin site has been mutated rendering this construct resistant to protease cleavage at this site. A recent preprint reporting cryo-EM structures of a full-length Omicron spike construct shows similar RBD-RBD interactions in the 3-RBD-down state as we have observed here, thus further supporting our spike
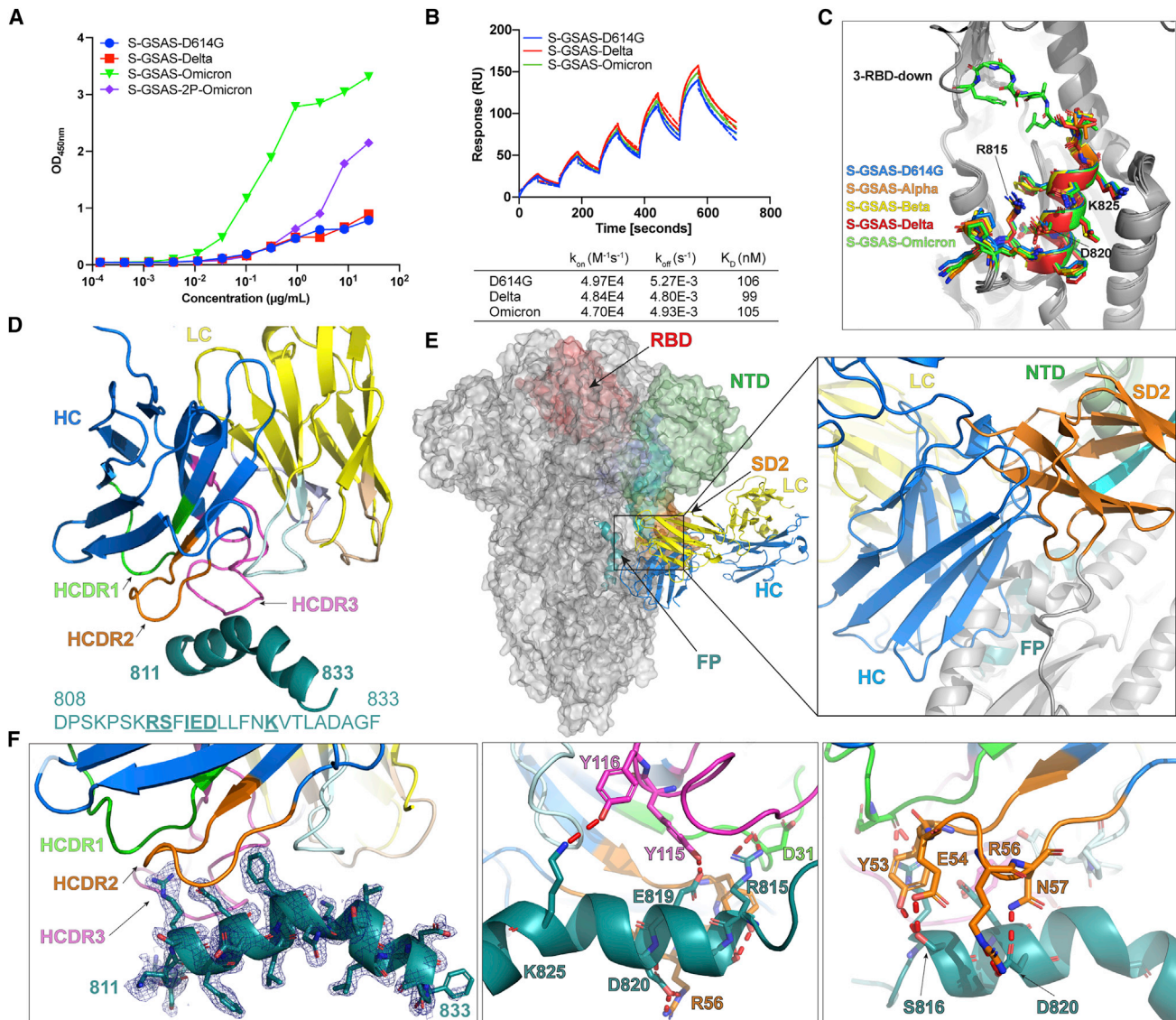
Figure 7. Binding of DH1058 to SARS-CoV-2 fusion peptide

(A) Binding of DH1058 to spike variants measured by ELISA.

(B) Kinetics and affinity of DH1058 Fabs binding to spike variants measured by SPR. The full lines are the binding sensorgrams and the dotted lines show fits of the data to a 1:1 Langmuir binding model. The on-rate (k_{on}, M^{-1} s^{-1}), off-rate (k_{off}, s^{-1}), and affinity (K_D, nM) for each interaction are indicated.

(C) Conservation of the FP conformation in variant S protein structures. S-GSAS-D614G (PDB 7KDK, blue), S-GSAS-Alpha (B.1.1.7, PDB 7LWS, orange), S-GSAS-Beta (B.1.351, PDB 7LYM, yellow), S-GSAS-Delta (B.1.617.2, PDB: 7TOU, red), and S-GSAS-Omicron (B.1.529, PDB: 7TF8, green) were superimposed in Pymol using the extra fit method and residues 909–1036.

(D) Crystal structure of DH1058 Fab variable region (heavy chain in blue and light chain in yellow) bound to a peptide comprising the SARS-CoV-2 S protein residues 808–833 (in teal). CDRs are colored green (HCDR1), orange (HCDR2), pink (HCDR3), wheat (LCDR1), pale purple (LCDR2), and pale blue (LCDR3).

(E) Model of DH1058 (colored in blue and yellow as in [D]) bound to pre-fusion SARS-CoV-2 S protein (PDB 7KDK). The S protein is shown as a surface with 2 protomers colored gray and the protomer used for alignment with the crystal structure of DH1058-FP complex has its S1 subunits colored pale green (NTD), cyan (N2R linker), red (RBD) and dark blue and orange (SD1 and SD2 respectively). The inset panel shows a clash between DH1058 HC and the SARS-CoV-2 SD2 subdomain. A clash is also observed for between the HC and the S2 subunit HR1 subdomain (in gray).

(F) Left: electron density of the peptide in the crystal structure bound to DH1058. Right: contacts (indicated by red dashed lines) between the DH1058 Fabs and the S2 peptide in the crystal structure.

See also Figure S6 and Table 5.

ectodomain construct as being representative of the full-length spike (Zhang et al., 2022). Structural and spectroscopic studies performed on the SARS-CoV-2 spike in the context of the native virion were also found consistent with spike populations observed by single particle cryo-EM (Yang et al., 2022; Lu et al., 2020; Ke et al., 2020). Similar studies performed on the

Table 5. X-ray data collection and refinements statistics for DH1058 Fab-SARS-CoV-2 fusion peptide (FP) crystal structure, related to Figure 7

	PDB 7TOW
Data collection	
Space group	P 1 21 1
Unit-cell dimensions	
a, b, c (Å)	53.9, 76.8, 119.8
α, β, γ (°)	90.0, 100.9, 90.0
Resolution (Å)	2.15–2.23 (2.15–38.96)
CC(1/2)	0.960 (0.993)
CC*	0.990 (0.998)
Rpim[a]	0.115 (0.035)
R-work[b]	0.169 (0.167)
R-free[b]	0.253 (0.234)
Overall R-sym[c]	0.075
I/σ(I)	5.4 (22.5)
Completeness (%)	95.1 (92.8)
Refinement	
No. reflection/unique	4,817 (48,437)
Molprobity	
Ramachandran favored	95.68
Ramachandran allowed	3.24
Ramachandran outlier	1.08
Rotamer outliers	4.44
Clash score	4.35
No. of water	793
RMSD	
Bond lengths (Å)	0.007
Bond angles (°)	0.94

Values outside parentheses are for the highest-resolution shell.
Values in parentheses are overall values.
[a]$R_{pim} = \Sigma_{hkl}[1/(n_{hkl} - 1)]^{1/2}\Sigma_j|I_j(hkl) - \langle I(hkl)\rangle| /\Sigma_{hkl} \Sigma_j I_j(hkl)$
[b]$R = \Sigma hkl||F_{obs}| - |F_{calc}||/\Sigma hkl|F_{obs}|$. R-free is calculated from 5% of the reflections excluded from refinement.
[c]$R_{sym} = \Sigma|I - \langle I\rangle|/\Sigma \langle I\rangle$, where I is the observed intensity, and $\langle I\rangle$ is the average intensity of multiple observations of symmetry-related reflections.

Omicron spike will be valuable to bridge the conformational states observed in our structural studies with the spike conformations adopted in the virion context.

The extent to which the stabilization of the 3-RBD-down state of the Omicron spike versus the direct effect of point mutations within antibody epitopes affects its properties of immune evasion would require further detailed studies, including deconvolution of the complex mutational landscape of the Omicron spike into subsets of mutations designed to address these questions. Additionally, further functional studies will be needed to fully understand the impact that these structural observations have on the properties of the virus, including transmissibility and immune evasion. While we see structural stabilization of the 3-RBD-down state mediated by the amino acid substitutions

acquired at the RBD-RBD interface, further functional evidence is needed to determine the extent to which the shifts in RBD orientations influence viral transmission or immune escape. Similarly, to determine the extent to which our structural observation of altered FP dynamics in the Omicron spike affects its transmissibility will require further testing via functional assays.

STAR★METHODS

Detailed methods are provided in the online version of this paper and include the following:

- KEY RESOURCES TABLE
- RESOURCE AVAILABILITY
  - Lead contact
  - Materials availability
  - Data and code availability
- EXPERIMENTAL MODEL AND SUBJECT DETAILS
  - Cell culture
- METHOD DETAILS
  - Plasmids
  - Protein purification
  - Negative-stain electron microscopy
  - Differential scanning fluorimetry
  - ELISA assays
  - Surface plasmon resonance
  - Cryo-EM
  - Vector-based structure analysis
  - Difference distance matrices (DDM)
  - Pseudovirus neutralization assay
  - X-ray crystallography
- QUANTIFICATION AND STATISTICAL ANALYSIS

AUTHOR CONTRIBUTIONS

DECLARATION OF INTERESTS

REFERENCES

Adams, P.D., Afonine, P.V., Bunkóczi, G., Chen, V.B., Davis, I.W., Echols, N., Headd, J.J., Hung, L.W., Kapral, G.J., Grosse-Kunstleve, R.W., et al. (2010). Phenix: a comprehensive Python-based system for macromolecular structure solution. Acta Crystallogr. D Biol. Crystallogr. *66*, 213–221.

Afonine, P.V., Poon, B.K., Read, R.J., Sobolev, O.V., Terwilliger, T.C., Urzhumtsev, A., and Adams, P.D. (2018). Real-space refinement inPHENIXfor cryo-EM and crystallography. Acta Crystallogr. D Struct. Biol. *74*, 531–544.

Cai, Y., Zhang, J., Xiao, T., Lavine, C.L., Rawson, S., Peng, H., Zhu, H., Anand, K., Tong, P., Gautam, A., et al. (2021). Structural basis for enhanced infectivity and immune evasion of SARS-CoV-2 variants. Science *373*, 642–648.

Cameroni, E., Bowen, J.E., Rosen, L.E., Saliba, C., Zepeda, S.K., Culap, K., Pinto, D., Vanblargan, L.A., De Marco, A., Di Iulio, J., et al. (2022). Broadly neutralizing antibodies overcome SARS-CoV-2 Omicron antigenic shift. Nature *602*, 664–670.

Cao, Y., Wang, J., Jian, F., Xiao, T., Song, W., Yisimayi, A., Huang, W., Li, Q., Wang, P., An, R., et al. (2022). Omicron escapes the majority of existing SARS-CoV-2 neutralizing antibodies. Nature *602*, 657–663.

Cerutti, G., Guo, Y., Liu, L., Zhang, Z., Liu, L., Luo, Y., Huang, Y., Wang, H.H., Ho, D.D., Sheng, Z., et al. (2021). Structural basis for antibody resistance to SARS-CoV-2 Omicron variant. bioRxiv. https://doi.org/10.1101/2021.12.21.473620.

Croll, T.I. (2018). ISOLDE: a physically realistic environment for model building into low-resolution electron-density maps. Acta Crystallogr. D Struct. Biol. *74*, 519–530.

Cui, Z., Liu, P., Wang, N., Fan, K., Zhu, Q., Wang, K., Chen, R., Feng, R., Jia, Z., Yang, M., et al. (2021). Structural and functional characterizations of altered infectivity and immune evasion of SARS-CoV-2 Omicron variant. bioRxiv. https://doi.org/10.1101/2021.12.29.474402.

Edwards, R.J., Mansouri, K., Stalls, V., Manne, K., Watts, B., Parks, R., Janowska, K., Gobeil, S.M.C., Kopp, M., Li, D., et al. (2021). Cold sensitivity of the SARS-CoV-2 spike ectodomain. Nat. Struct. Mol. Biol. *28*, 128–131.

Emsley, P., Lohkamp, B., Scott, W.G., and Cowtan, K. (2010). Features and development of Coot. Acta Crystallogr. D Biol. Crystallogr. *66*, 486–501.

Gilbert, P.B., Montefiori, D.C., Mcdermott, A.B., Fong, Y., Benkeser, D., Deng, W., Zhou, H., Houchens, C.R., Martins, K., Jayashankar, L., et al. (2022). Immune correlates analysis of the mRNA-1273 COVID-19 vaccine efficacy clinical trial. Science *375*, 43–50.

Gobeil, S.M., Janowska, K., Mcdowell, S., Mansouri, K., Parks, R., Manne, K., Stalls, V., Kopp, M.F., Henderson, R., Edwards, R.J., et al. (2021a). D614G mutation alters SARS-CoV-2 spike conformation and enhances protease cleavage at the S1/S2 junction. Cell Rep. *34*, 108630.

Gobeil, S.M., Janowska, K., Mcdowell, S., Mansouri, K., Parks, R., Stalls, V., Kopp, M.F., Manne, K., Li, D., Wiehe, K., et al. (2021b). Effect of natural mutations of SARS-CoV-2 on spike structure, conformation, and antigenicity. Science *373*, 760–764.

Goddard, T.D., Huang, C.C., Meng, E.C., Pettersen, E.F., Couch, G.S., Morris, J.H., and Ferrin, T.E. (2018). UCSF ChimeraX: meeting modern challenges in visualization and analysis. Protein Sci. *27*, 14–25.

Grant, B.J., Skjaerven, L., and Yao, X.Q. (2021). The Bio3D packages for structural bioinformatics. Protein Sci. *30*, 20–30.

Henderson, R., Edwards, R.J., Mansouri, K., Janowska, K., Stalls, V., Gobeil, S.M.C., Kopp, M., Li, D., Parks, R., Hsu, A.L., et al. (2020). Controlling the SARS-CoV-2 spike glycoprotein conformation. Nat. Struct. Mol. Biol. *27*, 925–933.

Hoffmann, M., Krüger, N., Schulz, S., Cossmann, A., Rocha, C., Kempf, A., Nehlmeier, I., Graichen, L., Moldenhauer, A.S., Winkler, M.S., et al. (2022). The Omicron variant is highly resistant against antibody-mediated neutralization: implications for control of the COVID-19 pandemic. Cell *185*, 447–456.e11.

Hsieh, C.L., Goldsmith, J.A., Schaub, J.M., Divenere, A.M., Kuo, H.C., Javanmardi, K., Le, K.C., Wrapp, D., Lee, A.G., Liu, Y., et al. (2020). Structure-based design of prefusion-stabilized SARS-CoV-2 spikes. Science *369*, 1501–1505.

Humphrey, W., Dalke, A., and Schulten, K. (1996). VMD: visual molecular dynamics. J. Mol. Graph. *14*, 33–8, 27.

Ke, Z., Oton, J., Qu, K., Cortese, M., Zila, V., Mckeane, L., Nakane, T., Zivanov, J., Neufeldt, C.J., Cerikan, B., et al. (2020). Structures and distributions of SARS-CoV-2 spike proteins on intact virions. Nature *588*, 498–502.

Li, D., Edwards, R.J., Manne, K., Martinez, D.R., Schafer, A., Alam, S.M., Wiehe, K., Lu, X., Parks, R., Sutherland, L.L., et al. (2021). In vitro and in vivo functions of SARS-CoV-2 infection-enhancing and neutralizing antibodies. Cell *184*, 4203–4219.e32.

Liebschner, D., Afonine, P.V., Baker, M.L., Bunkóczi, G., Chen, V.B., Croll, T.I., Hintze, B., Hung, L.W., Jain, S., Mccoy, A.J., et al. (2019). Macromolecular structure determination using X-rays, neutrons and electrons: recent developments in Phenix. Acta Crystallogr. D Struct. Biol. *75*, 861–877.

Lu, M., Uchil, P.D., Li, W., Zheng, D., Terry, D.S., Gorman, J., Shi, W., Zhang, B., Zhou, T., Ding, S., et al. (2020). Real-time conformational dynamics of SARS-CoV-2 spikes on virus particles. Cell Host Microbe *28*, 880–891.e8.

Martinez, D.R., Schafer, A., Gobeil, S., Li, D., De La Cruz, G., Parks, R., Lu, X., Barr, M., Stalls, V., Janowska, K., et al. (2022). A broadly cross-reactive antibody neutralizes and protects against sarbecovirus challenge in mice. Sci. Transl. Med. *14*, eabj7125.

Mccallum, M., Bassi, J., De Marco, A., Chen, A., Walls, A.C., Di Iulio, J., Tortorici, M.A., Navarro, M.J., Silacci-Fregni, C., Saliba, C., et al. (2021a). SARS-CoV-2 immune evasion by the B.1.427/B.1.429 variant of concern. Science *373*, 648–654.

Mccallum, M., De Marco, A., Lempp, F.A., Tortorici, M.A., Pinto, D., Walls, A.C., Beltramello, M., Chen, A., Liu, Z., Zatta, F., et al. (2021b). N-terminal domain antigenic mapping reveals a site of vulnerability for SARS-CoV-2. Cell *184*, 2332–2347.e16.

Mccallum, M., Walls, A.C., Sprouse, K.R., Bowen, J.E., Rosen, L.E., Dang, H.V., De Marco, A., Franko, N., Tilles, S.W., Logue, J., et al. (2021c). Molecular basis of immune evasion by the Delta and Kappa SARS-CoV-2 variants. Science *374*, 1621–1626.

Mccoy, A.J., Grosse-Kunstleve, R.W., Adams, P.D., Winn, M.D., Storoni, L.C., and Read, R.J. (2007). Phaser crystallographic software. J. Appl. Crystallogr. *40*, 658–674.

Ni, D., Lau, K., Turelli, P., Raclot, C., Beckert, B., Nazarov, S., Pojer, F., Myasnikov, A., Stahlnerg, H., and Trono, D. (2021). Structural analysis of the

Spike of the Omicron SARS-COV-2 variant by cryo-EM and implications for immune evasion. bioRxiv. https://doi.org/10.1101/2021.12.27.474250.

Otwinowski, Z., and Minor, W. (1997). Processing of X-ray diffraction data collected in oscillation mode. Methods Enzymol. 276, 307–326.

Pettersen, E.F., Goddard, T.D., Huang, C.C., Couch, G.S., Greenblatt, D.M., Meng, E.C., and Ferrin, T.E. (2004). UCSF Chimera – a visualization system for exploratory research and analysis. J. Comput. Chem. 25, 1605–1612.

Pinto, D., Park, Y.J., Beltramello, M., Walls, A.C., Tortorici, M.A., Bianchi, S., Jaconi, S., Culap, K., Zatta, F., De Marco, A., et al. (2020). Cross-neutralization of SARS-CoV-2 by a human monoclonal SARS-CoV antibody. Nature 583, 290–295.

Planas, D., Saunders, N., Maes, P., Guivel-Benhassine, F., Planchais, C., Buchrieser, J., Bolland, W.H., Porrot, F., Staropoli, I., Lemoine, F., et al. (2022). Considerable escape of SARS-CoV-2 Omicron to antibody neutralization. Nature 602, 671–675.

Punjani, A., Rubinstein, J.L., Fleet, D.J., and Brubaker, M.A. (2017). cryoSPARC: algorithms for rapid unsupervised cryo-EM structure determination. Nat. Methods 14, 290–296.

Mannar, D., Saville, J.W., Zhu, X., Srivastava, S.S., Berezuk, A.M., Tuttle, K.S., Marquez, A.C., Sekirov, I., and Subramaniam, S. (2022). SARS-CoV-2 Omicron variant: antibody evasion and cryo-EM structure of spike protein-ACE2 complex. Science 375, 760–764.

Scheres, S.H.W. (2012). RELION: Implementation of a Bayesian approach to cryo-EM structure determination. Journal of Structural Biology 180, 519–530. https://doi.org/10.1016/j.jsb.2012.09.006.

Scheres, S.H.W. (2016). Processing of Structurally Heterogeneous Cryo-EM Data in RELION. Methods in Enzymology 579, 125–157. https://doi.org/10.1016/bs.mie.2016.04.012.

Schmidt, F., Muecksch, F., Weisblum, Y., Da Silva, J., Bednarski, E., Cho, A., Wang, Z., Gaebler, C., Caskey, M., Nussenzweig, M.C., et al. (2022). Plasma neutralization of the SARS-CoV-2 Omicron variant. N. Engl. J. Med. 386, 599–601.

Schneider, C., Rasband, W., Eliceiri, K., et al. (2012). NIH Image to ImageJ: 25 years of image analysis (Nat Methods).

Schrödinger, L. (2015). The PyMOL Molecular Graphics System.

R: a language and environment for statistical computing (R Foundation for Statistical Computing). Vienna, Austria. https://www.R-project.org/.

Tortorici, M.A., Czudnochowski, N., Starr, T.N., Marzi, R., Walls, A.C., Zatta, F., Bowen, J.E., Jaconi, S., Di Iulio, J., Wang, Z., et al. (2021). Broad sarbecovirus neutralization by a human monoclonal antibody. Nature 597, 103–108.

Walls, A.C., Park, Y.J., Tortorici, M.A., Wall, A., Mcguire, A.T., and Veesler, D. (2020). Structure, function, and antigenicity of the SARS-CoV-2 Spike glycoprotein. Cell 181, 281–292.e6.

Williams, W.B., Meyerhoff, R.R., Edwards, R.J., Li, H., Manne, K., Nicely, N.I., Henderson, R., Zhou, Y., Janowska, K., Mansouri, K., et al. (2021). Fab-dimerized glycan-reactive antibodies are a structural category of natural antibodies. Cell 184, 2955–2972.e25.

Wrapp, D., Wang, N., Corbett, K.S., Goldsmith, J.A., Hsieh, C.L., Abiona, O., Graham, B.S., and Mclellan, J.S. (2020). Cryo-EM structure of the 2019-nCoV spike in the prefusion conformation. Science 367, 1260–1263.

Yang, Z., Han, Y., Ding, S., Shi, W., Zhou, T., Finzi, A., Kwong, P.D., Mothes, W., and Lu, M. (2022). SARS-CoV-2 variants increase kinetic stability of open spike conformations as an evolutionary strategy. mBio 13, e0322721.

Yuan, M., Wu, N.C., Zhu, X., Lee, C.D., So, R.T.Y., Lv, H., Mok, C.K.P., and Wilson, I.A. (2020). A highly conserved cryptic epitope in the receptor binding domains of SARS-CoV-2 and SARS-CoV. Science 368, 630–633.

Zhang, J., Xiao, T., Cai, Y., Lavine, C.L., Peng, H., Zhu, H., Anand, K., Tong, P., Gautam, A., Mayer, M.L., et al. (2021). Membrane fusion and immune evasion by the spike protein of SARS-CoV-2 Delta variant. Science 374, 1353–1360.

Zhang, J., Cai, Y., Lavine, C.L., Peng, H., Zhu, H., Anand, K., Tong, P., Gautam, A., Mayer, M.L., Ritts-Volloch, S., et al. (2022). Structural and functional impact by SARS-CoV-2 Omicron spike mutations. Cell Reports 39. https://doi.org/10.1016/j.celrep.2022.110729.

Zhou, T., Wang, L., Misasi, J., Pegu, A., Zhang, Y., Harris, D.R., Olia, A.S., Talana, C.A., Yang, E.S., Chen, M., et al. (2021). Structural basis for potent antibody neutralization of SARS-CoV-2 variants including B.1.1.529. bioRxiv. https://doi.org/10.1101/2021.12.27.47430.

Zivanov, J., Nakane, T., Forsberg, B.O., Kimanius, D., Hagen, W.J., Lindahl, E., and Scheres, S.H. (2018). New tools for automated high-resolution cryo-EM structure determination in RELION-3. eLife 7, e42166.

STAR★METHODS

KEY RESOURCES TABLE

REAGENT or RESOURCE	SOURCE	IDENTIFIER
Antibodies		
ACE2	Henderson et al. (2020)	N/A
CR3022	Henderson et al. (2020)	N/A
2G12	Williams et al. (2021)	N/A
Goat anti-rabbit-HRP	Abcam	ab97080
Goat anti-human-HRP	Jackson ImmunoResearch Laboratories	109-035-098
Mouse anti-monkey IgG HRP	Southern Biotech	Cat #:4700-05; RRID:AB_2796069
DH1050.1	Li et al. (2021)	N/A
DH1052	Li et al. (2021)	N/A
S309	Pinto et al. (2020)	N/A
DH1041	Li et al. (2021)	N/A
DH1042	Li et al. (2021)	N/A
DH1047	Li et al. (2021)	N/A
S2X259	Tortorici et al. (2021)	N/A
DH1044	Li et al. (2021)	N/A
DH1193	Li et al. (2021)	N/A
DH1058	Li et al. (2021)	N/A
Bacterial and virus strains		
Spike-pseudotyped virus D614G (B.1)	David Montefiori & Xiaoying Shen, Duke	N/A
Spike-pseudotyped virus Omicron (B.1.1.529)	David Montefiori & Xiaoying Shen, Duke	N/A
Chemicals, peptides, and recombinant proteins		
FreeStyle 293 Expression Medium	GIBCO	12338018
Expi293 Expression Medium	GIBCO	A1435101
ExpiFectamine 293 Transfection Kit	GIBCO	A14524
Hyclone SFM4HEK293	Cytiva	SH30521.02
Opti-MEM I	GIBCO	31985-070
Turbo293	Speed BioSystems	PXX1002
10x Buffer E	IBA	2-1000
10x Buffer R	IBA	2-1002
10x Buffer W	IBA	2-1003
Strep-Tactin resin	IBA	2-1201
8% Glutaraldehyde	Electron Microscopy Sciences	16019
300mesh Cu carbon coated	Electron Microscopy Sciences	CF300-Cu
Uranyl formate	Electron Microscopy Sciences	22450 S-888
Quantifoil R 1.2/1.3 300 mesh	Electron Microscopy Sciences	Q350CR-14
Streptavidin	Thermo Fisher Scientific	S-888
Streptavidin-HRP	Thermo Scientific	Ref #21132
D-mannose	Sigma	CAS #:3458-28-4
Tween 20	Sigma	P7949
Phosphate Buffered Saline (25x) pH 7.6	ScyTek Laboratories	PBS-20000

(Continued on next page)

Continued

REAGENT or RESOURCE	SOURCE	IDENTIFIER
Sodium Bicarbonate	Sigma	S6297
Sodium Azide	Sigma	S8032
Hydrochloric Acid	Fischer Scientific	A142-212
Whey Protein	Bipro USA	Unflavored Whey
Goat Serum	Invitrogen	16210-072
SureBlue Reserve TMB	KPL	53-00-03
Bovine Serum Albumin	Sigma	A3059
Critical commercial assays		
Superose 6 Increase 10/300 GL	Cytiva	29091596
NuPage 4-12%	Invitrogen	NP0321
TMB substrate	Sera Care Life Sciences	5120-0083
Luciferase Cell Culture Lysis 5x Reagent	Promega	Cat# E1531
Bright-Glo Luciferase Assay System	Promega	Cat# #2650
Deposited data		
SARS-CoV-2 Omicron 3-RBD down Spike Protein Trimer without the P986-P987 stabilizing mutations (S-GSAS-Omicron)	This study	PDB: 7TF8; EMDB: 25865
SARS-CoV-2 Omicron 3-RBD down Spike Protein Trimer without the P986-P987 stabilizing mutations (S-GSAS-Omicron)	This study	PDB: 7TL1; EMDB: 25983
SARS-CoV-2 Omicron 1-RBD up Spike Protein Trimer without the P986-P987 stabilizing mutations (S-GSAS-Omicron)	This study	PDB 7TEI; EMDB: 25846
SARS-CoV-2 Omicron 1-RBD up Spike Protein Trimer without the P986-P987 stabilizing mutations (S-GSAS-Omicron)	This study	PDB 7TL9; EMDB: 25984
SARS-CoV-2 Omicron 1-RBD down Spike Protein Trimer without the P986-P987 stabilizing mutations (S-GSAS-Omicron)	This study	PDB 7TGE; EMDB: 25880
SARS-CoV-2 Omicron-BA.1 2-RBD up Spike Protein Trimer without the P986-P987 stabilizing mutations (S-GSAS-Omicron-BA.1)	This study	EMDB: 26600
Delta (B.1.617.2) SARS-CoV-2 variant spike protein (S-GSAS-Delta) in the 3-RBD-down conformation; consensus state D1	This study	PDB 7TOU; EMDB: 26038
Delta (B.1.617.2) SARS-CoV-2 variant spike protein (S-GSAS-Delta) in the 3-RBD-down conformation; Subclassification D5 state	This study	PDB 7TOX; EMDB: 26040
Delta (B.1.617.2) SARS-CoV-2 variant spike protein (S-GSAS-Delta) in the 3-RBD-down conformation; Subclassification D6 state	This study	PDB 7TOY; EMDB: 26041
Delta (B.1.617.2) SARS-CoV-2 variant spike protein (S-GSAS-Delta) in the 3-RBD-down conformation; Subclassification D8 state	This study	PDB 7TP0; EMDB: 26043
Delta (B.1.617.2) SARS-CoV-2 variant spike protein (S-GSAS-Delta) in the 3-RBD-down conformation; Subclassification D9 state	This study	PDB 7TP1; EMDB: 26045
Delta (B.1.617.2) SARS-CoV-2 variant spike protein (S-GSAS-Delta) in the 3-RBD-down conformation; Subclassification D10 state	This study	PDB 7TP2; EMDB: 26046
Delta (B.1.617.2) SARS-CoV-2 variant spike protein (S-GSAS-Delta) in the 1-RBD-up conformation; consensus state D2	This study	PDB 7TOV; EMDB: 26039
Delta (B.1.617.2) SARS-CoV-2 variant spike protein (S-GSAS-Delta) in the 1-RBD-up conformation; Subclassification D11 state	This study	PDB 7TP7; EMD: 26047
Delta (B.1.617.2) SARS-CoV-2 variant spike protein (S-GSAS-Delta) in the 1-RBD-up conformation; Subclassification D12 state	This study	PDB 7TP8; EMDB: 26048
Delta (B.1.617.2) SARS-CoV-2 variant spike protein (S-GSAS-Delta) in the 1-RBD-up conformation; Subclassification D13 state	This study	PDB 7TP9; EMDB: 26049
Delta (B.1.617.2) SARS-CoV-2 variant spike protein (S-GSAS-Delta) in the 1-RBD-up conformation; Subclassification D14 state	This study	PDB 7TPA; EMDB: 26050
Delta (B.1.617.2) SARS-CoV-2 variant spike protein (S-GSAS-Delta) in the 1-RBD-up conformation; Subclassification D15 state	This study	PDB 7TPC; EMDB: 26051
Delta (B.1.617.2) SARS-CoV-2 variant spike protein (S-GSAS-Delta) in the 1-RBD-up conformation; Subclassification D16 state	This study	PDB 7TPE; EMDB: 26052

(Continued on next page)

Continued

REAGENT or RESOURCE	SOURCE	IDENTIFIER
Delta (B.1.617.2) SARS-CoV-2 variant spike protein (S-GSAS-Delta) in the 1-RBD-up conformation; Subclassification D17 state	This study	PDB 7TPF; EMDB: 26053
Delta (B.1.617.2) SARS-CoV-2 variant spike protein (S-GSAS-Delta) in the 2-RBD-up conformation - D3	This study	PDB: 7TPH; EMDB: 26055
Delta (B.1.617.2) SARS-CoV-2 variant spike protein (S-GSAS-Delta) in the M1 conformation, D4	This study	PDB: 7TPL; EMDB: 26059
Antibody DH1058 Fab fragment bound to SARS-CoV-2 fusion peptide	This study	PDB: 7TOW
Down-state locked rS2d SARS-CoV-2 spike ectodomain in the RBD-down conformation, State 1	This study	PDB 7TLA; EMDB: 25985
Down-state locked rS2d SARS-CoV-2 spike ectodomain in the RBD-down conformation, State 2	This study	PDB 7TLB; EMDB: 25986
Down-state locked, S2 stabilized rS2d-HexaPro SARS-CoV-2 spike ectodomain in the RBD-down conformation, State 1	This study	PDB 7TLC; EMDB: 25987
Down-state locked, S2 stabilized rS2d-HexaPro SARS-CoV-2 spike ectodomain in the RBD-down conformation, State 2	This study	PDB 7TLD; EMDB: 25988
CryoEM structure of SARS-CoV-2 S protein in complex with Receptor Binding Domain antibody DH1042	This study	PDB 7THT; EMDB: 25904
Structure of RBD directed antibody DH1042 in complex with SARS-CoV-2 spike: Local refinement of RBD-Fab interface	This study	PDB 7THE; EMDB: 25893
Video S1: Morph between rS2d-HexaPro States 1 and 2.	This study	Mendeley Data: https://data.mendeley.com/datasets/kxjf56yy6d/1
Experimental models: Cell lines		
Freestyle 293-F cells	GIBCO	R79007
Expi293F cells	GIBCO	A14527
293T/ACE2 cells	Drs. Mike Farzan and Huihui Mu, Scripps	N/A
HEK293T/17	ATCC	CRL-11268
Recombinant DNA		
pαH-S-GSAS/D614G	Gobeil et al., 2021a	Addgene 164566
paH-S-GSAS-OMICRON	This study	Addgene 180423
paH-S-GSAS-2P-OMICRON	This study	Addgene 180593
paH-S-GSAS-B.1.617.2.v1	This study	Addgene 182575
rS2d-HexaPro	This study	Addgene 183515
rS2d	This study	Addgene 183516
Software and algorithms		
Relion	Scheres, 2012; Scheres, 2016	Version 3.1
cryoSPARC	Punjani et al. (2017)	https://cryosparc.com
Phenix	Afonine et al. (2018), Liebschner et al. (2019)	Version 1.17
Coot	Emsley et al. (2010)	Version 0.8.9.2
Pymol	Schrodinger The PyMOL Molecular Graphics System (Schrödinger, 2015).	https://www.pymol.org/
UCSF Chimera	Pettersen et al. (2004)	http://www.cgl.ucsf.edu/chimera/
Chimera X	Goddard et al. (2018)	https://www.rbvi.ucsf.edu/chimerax/
Image Lab	Bio-Rad	Version 6.0
PRISM 8	GraphPad Software	Version 8.4.0

(Continued on next page)

Continued

REAGENT or RESOURCE	SOURCE	IDENTIFIER
R	R Core Team (2018). R: A language and environment for statistical computing. R Foundation for Statistical Computing, Vienna, Austria. URL http://www.R-project.org/	version 4.0.2
Softmax Pro	Molecular Devices	Version 5.3
Bio3D	Grant et al. (2021)	Version 2.4-1
ImageJ	Schneider et al., 2012	Version 1.53a
Sequencher (Version 5.4.6)	Gene Codes Corporation	www.Genecodes.com

RESOURCE AVAILABILITY

Lead contact
Further information and requests for resources and reagents should be directed to and will be fulfilled by the Lead Contact, Priyamvada Acharya (priyamvada.acharya@duke.edu).

Materials availability
Further information and requests for resources and reagents should be directed to Priyamvada Acharya (priyamvada.acharya@duke.edu). Plasmids generated in this study have been deposited to Addgene under the codes 180423, 180593, 182575, 183515, 183516.

Data and code availability
- Cryo-EM reconstructions and atomic models generated during this study are available at wwPDB and EMBD (https://www.rcsb.org; http://emsearch.rutgers.edu) under the accession codes PDB: 7TF8, 7TL1, 7TEI, 7TL9, 7TGE, 7TOU, 7TOX, 7TOY, 7TOZ, 7TP0, 7TP1, 7TP2, 7TOV, 7TP7, 7TP8, 7TP9, 7TPA, 7TPC, 7TPE, 7TPF, 7TPH, 7TPL, 7TLA, 7TLB, 7TLC, 7TLD, 7THT and 7THE, and EMDB: 25865, 25983, 25846, 25984, 25880, 26038, 26040, 26041, 26042, 26043, 26045, 26046, 26039, 26047, 26048, 26600, 26049, 26050, 26051, 26052, 26053, 26055, 26059, 25985, 25986, 25987, 25988, 25904 and 25893. The crystal structure of DH1058 Fab bound to the SARS-CoV-2 fusion peptide is deposited at wwPDB with accession code PDB: 7TOW.
- This paper does not report original code.
- Any additional information required to reanalyze the data reported in this paper is available from the lead contact upon request.

EXPERIMENTAL MODEL AND SUBJECT DETAILS

Cell culture
Gibco FreeStyle 293-F cells (embryonal, human kidney) were incubated at 37°C and 9% CO_2 in a humidified atmosphere. Cells were incubated in FreeStyle 293 Expression Medium (Gibco) with agitation at 120 rpm. Plasmids were transiently transfected into cells using Turbo293 (SpeedBiosystems) and incubated at 37 °C, 9% CO2, 120 rpm for 6 days. On the day following transfection, HyClone CDM4HEK293 media (Cytiva, MA) was added to the cells.

Antibodies were produced in Expi293 cells (embryonal, human kidney). Cells were incubated in Expi293 Expression Medium at 37°C, 120 rpm and 8% CO_2 in a humidified atmosphere. Plasmids were transiently transfected into cells using the ExpiFectamine 293 Transfection Kit and protocol (Gibco).

METHOD DETAILS

Plasmids
Mutagenesis of all plasmids generated in this study was performed and sequences confirmed by GeneImmune Biotechnology (Rockville, MD). The SARS-CoV-2 S protein ectodomain constructs comprised S protein residues 1 to 1208 (GenBank: MN908947) with the D614G mutation, the furin cleavage site (RRAR; residue 682-685) mutated to GSAS, a C-terminal T4 fibritin trimerization motif, a C-terminal HRV3C protease cleavage site, a TwinStrepTag and an 8XHisTag. All S ectodomains were cloned into the mammalian expression vector pαH and have been deposited to Addgene (https://www.addgene.org).

Protein purification

Spike ectodomains were harvested from concentrated supernatant on the 6th day post transfection and purified using StrepTactin resin (IBA LifeSciences) followed by size exclusion chromatography (SEC) using a Superose 6 10/300 GL Increase column (Cytiva, MA) equilibrated in 2mM Tris, pH 8.0, 200 mM NaCl, 0.02% NaN_3. All purification steps were performed at room temperature and were completed the same day that the supernatant was harvested. Protein quality was assessed by SDS-PAGE using NuPage 4-12% gels (Invitrogen, CA). The purified proteins were flash frozen and stored at -80°C in single-use aliquots. Each aliquot was thawed before use by placing at 37 °C for 20 minutes. Antibodies were produced in Expi293F cells, purified by Protein A affinity chromatography, and digested using LysC to generate Fab fragments. ACE2 with human Fc tag was purified by Protein A affinity chromatography and SEC.

Negative-stain electron microscopy

Fab-spike complex of DH1044 was generated by mixing 5.9 μg of spike with 6.2 μg of Fab in ~25 μl of HEPES-buffered saline (HBS) containing 20 mM HEPES and 150 mM NaCl, pH 7.4, and incubating at 37 °C for 1 hr and using sample directly for negative stain without further purification. Fab-spike complex of DH1193 was generated by mixing 20 μg of spike with 28 μg of Fab in ~200 μl of phosphate-buffered saline and incubating 1 hr at 37 °C. Sample was then brought to room temperature and diluted with 800 μl HBS, mixed, and then diluted with HBS augmented with 16 mM glutaraldehyde (Electron Microscopy Sciences, PA), fixed for 5 min, quenched by addition of 40 μl of 1 M Tris buffer, pH 7.4, and concentrated in a 2-ml 100-kDa MWCO Amicon centrifugal concentrator by spinning 10 min at 4000 rpm in a Sorvall benchtop centrifuge with a swinging-bucket rotor, yielding a final volume of ~75 μl. Protein concentration was measured using a Nanodrop which reported a nominal spike concentration of 0.6 mg/ml. For negative stain, samples were diluted to 0.1 mg/ml with HBS augmented with 5 g/dl glycerol and 8 mM glutaraldehyde. After 5 min incubation, excess glutaraldehyde was quenched by adding sufficient 1 M Tris stock, pH 7.4, to give 75 mM final Tris concentration and incubated for 5 min. Quenched sample was applied to a glow-discharged carbon-coated EM grid (Electron Microscopy Sciences, PA, CF300-Cu) for 10-12 second, then blotted, and stained with 2 g/dL uranyl formate (Electron Microscopy Sciences, PA), for 1 min, blotted and air-dried. Grids were examined on a Philips EM420 electron microscope operating at 120 kV and images were collected at a nominal magnification of 82,000x on a 4 Mpix CCD camera at 4.02 Å/pixel for DH1044 data, or at 49,000x on a 76 Mpix CCD camera at 2.4 Å/pixel for DH1193 data. Images were analyzed and 3D reconstructions generated using standard protocols with Relion 3.0 (Zivanov et al., 2018).

Differential scanning fluorimetry

DSF assays were performed using Tycho NT. 6 (NanoTemper Technologies). S protein ectodomains were diluted to approximatively 0.15 mg/ml. Intrinsic fluorescence was measured at 330 nm and 350 nm while the sample was heated from 35 to 95 °C at a rate of 30°C/min. The ratio of fluorescence (350/330 nm) and inflection temperatures (Ti) were calculated by the Tycho NT. 6 software.

ELISA assays

Spike ectodomains tested for antibody- or ACE2-binding in ELISA assays as previously described (Edwards et al., 2021). Briefly, serially diluted spike protein was bound in wells of a 384-well plates, which were previously coated with streptavidin (Thermo Fisher Scientific, MA) at 2 μg/mL and blocked. Proteins were incubated at room temperature for 1 hour, washed, then human mAbs were added at 10 μg/ml. Antibodies were incubated at room temperature for 1 hour, washed and binding detected with goat anti-human-HRP (Jackson ImmunoResearch Laboratories, PA) and TMB substrate.

Recombinant FDG mAbs were tested for binding to the SARS-CoV-2 Omicron spike (S-GSAS-Omicron, Lot: 486KJ), Delta spike (S-GSAS/B.1.617.2.v1, Lot: 076XH), SARS-CoV-2 spike (nCoV-1_2 ProRev+D614G, Lot: 001AM), in ELISA in the absence or presence of single monomer D-mannose as previously described (PMID: 34019795). Briefly, spike proteins (20ng) were captured by streptavidin (30ng per well) to individual wells of a 384-well Nunc-absorb ELISA plates using PBS-based buffers and assay conditions as previously described (PMID: 34019795; PMID: 28298421; PMID: 28298420). Commercially obtained D-mannose (Sigma, St. Louis, MO) was used to outcompete mAb binding to glycans on the spike proteins; D-mannose solutions were also produced in ELISA PBS-based glycan buffers at a concentration of [1M] D-mannose as described (PMID: 34019795). Mouse anti-monkey IgG-HRP (Southern Biotech, CAT# 4700-05) and Goat anti-human IgG-HRP (Jackson ImmunoResearch Laboratories, CAT# 109-035-098) secondary antibodies were used to detect antibody bound to the spike proteins. HRP detection was subsequently quantified with 3,30,5,50-tetramethylbenzidine (TMB) by measuring binding levels at an absorbance of 450nm, and binding titers were also reported as Log area under the curve (AUC).

Surface plasmon resonance

Antibody binding to SARS-CoV-2 S protein ectodomains was assessed on a Biacore T-200 (Cytiva, MA, formerly GE Healthcare) with HBS buffer supplemented with 3 mM EDTA and 0.05% surfactant P-20 (HBS-EP+, Cytiva, MA). Assays were performed at 25°C. S protein variants were captured on a Series S Strepavidin (SA) chip (Cytiva, MA) coated at 100 nM (60s at 10μL/min). Fabs were injected at concentrations ranging from 0.625 nM to 800 nM (prepared in a 2-fold serial dilution manner) over the S proteins using the

single cycle kinetics mode with 5 concentrations per cycle. The surface was regenerated after the last injection with 3 pulses of a 50mM NaoH + 1M NaCl solution for 10 seconds at 100µL/min. Sensogram data were analyzed using the BiaEvaluation software (Cytiva, MA)

Cryo-EM

Purified SARS-CoV-2 S protein ectodomains were diluted to a concentration of ∼1.5 mg/mL in 2 mM Tris pH 8.0, 200 mM NaCl and 0.02% NaN$_3$ and 0.5% glycerol was added. A 2.3-µL drop of protein was deposited on a Quantifoil-1.2/1.3 grid (Electron Microscopy Sciences, PA) that had been glow discharged for 10 seconds using a PELCO easiGlow™ Glow Discharge Cleaning System. After a 30-second incubation in >95% humidity, excess sample was blotted away from the grid for 2.5 seconds using a Whatman 1 filter paper before being plunged into liquid ethane using a Leica EM GP2 plunge freezer (Leica Microsystems). Frozen grids were imaged using a Titan Krios (Thermo Fisher) equipped with a K3 detector (Gatan). The cryoSPARC (Punjani et al., 2017) software was used for data processing. Phenix (Liebschner et al., 2019, Afonine et al., 2018), Coot (Emsley et al., 2010), Pymol (Schrödinger, 2015), Chimera (Pettersen et al., 2004), ChimeraX (Goddard et al., 2018) and Isolde (Croll, 2018) were used for model building and refinement.

Vector-based structure analysis

Vector analysis of intraprotomer and interprotomer domain positions was performed as described previously (Henderson et al., 2020) using the Visual Molecular Dynamics (VMD) (Humphrey et al., 1996) software package Tcl interface. Briefly, for each protomer of each structure, Cα centroids were determined for the NTD, a region at the base of the NTD near SD2 and the SD1 of an adjacent protomer referred to as the NTD′, SD1, SD2, CD, and a S2 sheet motif. Additional centroids for the NTD and RBD were determined for use as reference points for monitoring the relative NTD and RBD orientations to the NTD′ and SD1, respectively. Vectors were calculated between structurally related domain centroids and used to determine domain to domain distances and angles, and dihedrals were determined from these vectors and centroids. Principal components analysis and K-means clustering of the vector sets was performed in R (R Core Team, 2018). Data were centered and scaled for the PCA analyses.

Difference distance matrices (DDM)

DDM were generated using the Bio3D package (Grant et al., 2021) implemented in R (R Core Team, 2018. R: A language and environment for statistical computing. R Foundation for StatisticalComputing, Vienna, Austria. http://www.R-project.org/).

Pseudovirus neutralization assay

The pseudovirus neutralization assay performed at Duke has been described in detail (Gilbert et al., 2022) and is a formally validated adaptation of the assay utilized by the Vaccine Research Center; the Duke assay is FDA approved for D614G. For measurements of neutralization, pseudovirus was incubated with 8 serial 5-fold dilutions of antibody samples (1:20 starting dilution using antibodies diluted to 1.0 mg/ml) in duplicate in a total volume of 150 µl for 1 hr at 37°C in 96-well flat-bottom culture plates. 293T/ACE2-MF cells were detached from T75 culture flasks using TrypLE Select Enzyme solution, suspended in growth medium (100,000 cells/ml) and immediately added to all wells (10,000 cells in 100 µL of growth medium per well). One set of 8 wells received cells + virus (virus control) and another set of 8 wells received cells only (background control). After 71-73 hrs of incubation, medium was removed by gentle aspiration and 30 µl of Promega 1X lysis buffer was added to all wells. After a 10-minute incubation at room temperature, 100 µl of Bright-Glo luciferase reagent was added to all wells. After 1-2 minutes, 110 µl of the cell lysate was transferred to a black/white plate. Luminescence was measured using a GloMax Navigator luminometer (Promega). Neutralization titers are the inhibitory dilution (ID) of serum samples at which RLUs were reduced by 50% (ID50) compared to virus control wells after subtraction of background RLUs. Serum samples were heat-inactivated for 30 minutes at 56°C prior to assay.

X-ray crystallography

After size exclusion purification, DH1058 fab was concentrated to 26 mg/mL. The fusion peptide fragment was solubilized in PBS + 10% DMSO at a concentration of 10 mg/mL. The protein and the peptide were mixed at a Fab:peptide molar ratio of 1:2. Crystals were grown in 20% PEG3000, 100mM Tris base/HCl pH 7.0, 200mM calcium acetate at 22°C in a sitting drop vapor diffusion setting using a drop ratio of 0.4 µL protein : 0.2 µL reservoir solution. Large UV-active plate shaped crystals were observed after 24 hours. A single crystal was cryopreserved directly from the drop. Diffraction data was collected at the Advanced Photon Source using sector 22ID beamline. The collected diffraction images were indexed, integrated, and scaled using HKL2000 (Otwinowski and Minor, 1997) Initial phases were calculated by molecular replacement using Phenix.PHASER (Adams et al., 2010; McCoy et al., 2007) and the PDB 5GGU (Crystal structure of tremelimumab Fab) as a search model. Iterative rounds of manual model building using Coot (Emsley et al., 2010) and automatic refinement in PHENIX (Liebschner et al., 2019; Afonine et al., 2018) were performed. Data collection and refinement statistics are summarized in Table 5. The refined structure has been deposited to the Protein Data Bank (http://www.pdb.org) under the accession code 7TOW.

QUANTIFICATION AND STATISTICAL ANALYSIS

No statistical analyses were performed in this study.